

Deformable Mirror Demonstration

Kristin Berry

Ashley K. Carlton

Zachary J. Casas

James R. Clark

Vladimir Eremin

Zaira G. Garate

Julian Lemus

Immanuel David Madukauwa-David

Tam Nguyen T. Nguyen

Paul Salcido

Alexandra E. Wassenberg

May 6, 2013

Contents

1	Introduction	6
1.1	Mission Statement	6
1.2	Motivation	6
2	Mission Overview	6
2.1	Requirements	6
2.2	Concept of Operations -ZG	6
2.3	N^2 Diagram	7
2.4	System Level Budgets	8
2.4.1	Mass	8
2.4.2	Power	8
3	Subsystems	8
3.1	Payload	8
3.1.1	Requirements - AC	8
3.1.2	Trade Studies and Decisions Made - AC and KB	10
3.1.3	Analysis	16
3.1.4	Summary of Outputs - AC	16
3.1.5	Requirements	17
3.1.6	Trade Studies and Decisions Made	17
3.1.7	Analysis	17
3.1.8	Summary of Outputs	17
3.1.9	Risks	18
3.1.10	Future Work - AC	18
3.2	Power - JC	18
3.2.1	Requirements	18
3.2.2	Trade Studies and Decisions Made	18
3.2.3	Decisions Made	19
3.2.4	Analysis	20
3.2.5	Summary of Outputs	22
3.2.6	Risks	23
3.2.7	Future Work	24
3.3	Communication	25

3.3.1	Requirements - ZC	25
3.3.2	Trade Studies - ZC	25
3.3.3	Decisions Made - ZC	26
3.3.4	Analysis - ZC	27
3.3.5	Summary of Outputs - ZC	31
3.3.6	Risks - ZC	32
3.3.7	Future Work - ZC	32
3.4	Avionics	32
3.4.1	Requirements - VE	32
3.4.2	Trade Studies - VE	32
3.4.3	Decisions Made - VE	34
3.4.4	Analysis - VE	34
3.4.5	Summary of Outputs - ZC	34
3.4.6	Risks - ZC	35
3.4.7	Future Work - ZC	36
3.5	Attitude Determination and Control System	37
3.6	Thermal - Tam? David?	37
3.6.1	Requirements	37
3.6.2	Analysis/Results	37
3.6.3	Trade Studies	38
3.6.4	Design/Budget	39
3.7	Structures	41
4	Conclusion - AW	41
4.1	Risk Summary - AW	41
4.2	Future Work - AW	42
4.3	Attitude Determination and Control System (ADCS) - TN	43
4.3.1	Requirements	43
4.3.2	Trade Studies	43
4.3.3	Decision Made	44
4.3.4	Analysis	46
4.3.5	Summary of Budgets	48
4.3.6	Risks	48
4.3.7	Future Work	49
4.4	Thermal	51

4.5	Structure	51
5	Conclusion	51
5.1	Risk Analysis	51
5.2	Future Work	51
6	Acknowledgment	51
A		
	Requirements	52
B		
	Link Budgets	53

List of Figures

1	Timeline of the concept of operations for the DeMi Mission	6
2	High-Level N^2 diagram showing input/output relationships between subsystems	7
3	System Mass Budget	9
4	System Power Budget	10
5	This is the Michelson Interferometer with the flat mirror on a linear stager. This is a payload design possibility.	11
6	This is the Wavefront Sensing design with a Shack-Hartmann lenslet array. This is a payload design possibility.	12
7	This figure demonstrates the result of two wavefronts, plane and aberrated, entering a Shack-Hartmann lenslet array, and their resulting spot diagrams on the detector.	16
8	This is the MLA150 lenslet array from ThorLabs chosen for the Shack- Hartmann Wavefront Sensing design.	17
9	The “face-first” and “corner-first” attitudes. Images generated from STK. . .	19
10	The solar panel configuration to be used on the DeMi satellite. Image from Clyde Space.[1]	20
11	A “hot” orbit, where the satellite is exposed to the sun 80% of the time. Image generated from STK.	22
12	A “cold” orbit, where the satellite is exposed to the sun 63% of the time. Image generated from STK.	23

13	Photo of the custom-designed high-speed L3 Cadet radio [9].	26
14	Photo of stored and deployed measuring tape antenna. The pictured CubeSat has four antennas. DeMi will only be using one [11].	27
15	Diagram of propagation path of a signal from a satellite [12].	28
16	Representation of Satellite and Ground Station during Best Case Communication.	30
17	Representation of Satellite and Ground Station during Worst Case Communication.	31
18	Mission Interface Computer CS-MIC-G-EM [15]	34
19	Caption goes here...	36
20	Thermal environment of satellite considered in analysis.	37
21	Thermofoil heater and payload detector	38
22	Power usage by heater during different modes of operation.	39
23	Temperature decay of inner face of MLI for different modes of operation. . .	39
24	Precision Thermistor elements model 44004 (Omega.com).	40
25	Systems level risk chart.	42
26	Satellite orientation with respect to nadir direction and velocity vector . . .	45
27	ADCS components interactions and Avionics interface	47
28	Momentum and magnetic moment during detumbling period	49
29	Ground access STK model	50
30	Uplink Budget	53
31	Downlink Budget	54

List of Tables

1	This is a summary of the mass totals, power needs, and thermal needs of the major payload components.	17
2	Power values for various panel configurations and satellite attitudes.	19
3	Outputs to other systems (mass, volume, power consumed, and survival and operating temperatures).[3] [4] [5] [6]	24
4	Communications Trade Study for Maximum Downlink Data Rate	25
5	Communications Budgets	31
6	Hardware Options	33
7	Payload image capturing modes	33

8	Avionics hardware interfaces with other subsystems (*assuming update 10 times per second).	35
9	This is a summary of the mass totals, power needs, and thermal needs of the avionics system.	35
10	Operating and survival temperatures of different subsystems and components.	38
11	Results of the thermal analysis for hot and cold cases.	38
12	Key components and their corresponding number of thermal sensors required.	40
13	Outputs (mass, power consumed, volume) to other subsystems.	40
14	ADCS Sensors and Actuators	45
15	Torque coils specifications	46
16	Maximum Environmental Torque Estimation	47
17	ADCS budgets	50

List of Acronyms

DeMi Deformable Mirror Demonstration

DM Deformable Mirror

FOV Field of View

PSF Point Spread Function

1 Introduction

1.1 Mission Statement

1.2 Motivation

2 Mission Overview

2.1 Requirements

2.2 Concept of Operations -ZG

DeMi will be a 3-unit CubeSat on a low-Earth orbit with an altitude of 500 km at an inclination of 40. Immediately separation from a standard Poly-PicoSatellite Orbital Deployer (P-POD), the satellite will begin to charge its primary batteries through solar panels covering the long faces of the structure. During this first stage, the satellites antenna will be deployed and will emit intermittent signals, or beacons, in order to be located by the ground station. The ADCS torque coils will detumble the satellite and align it in a nadir-pointing position. The detumble stage should last approximately 2 weeks. In case the satellite needs more time to power up, communicate with the ground station and stabilize itself, the science operations could be delayed.

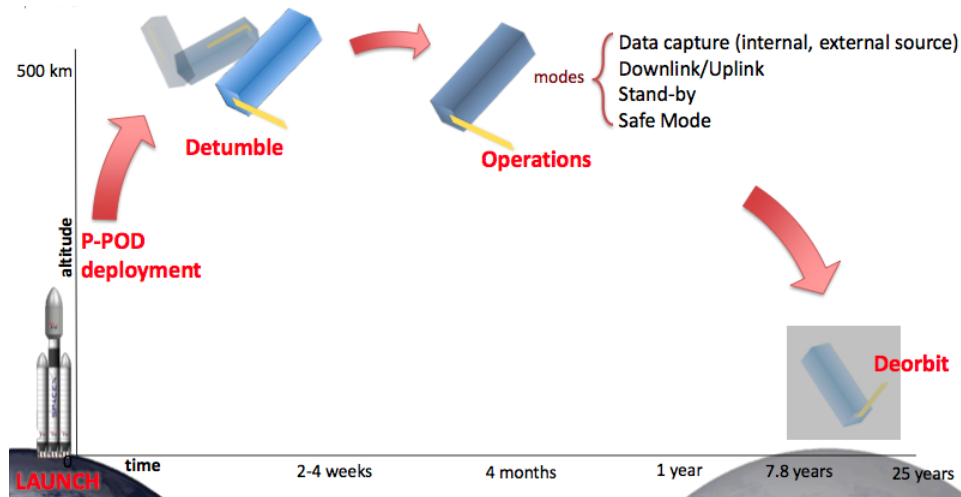


Figure 1: Timeline of the concept of operations for the DeMi Mission

Once the satellite is in fully operational status, the payload will begin to conduct its scientific experiments and collect data. Two different data capture modes will be performed

during the mission: internal source experiments will be done during the first 3 months of operations, while external source experiments will occur during the remainder of the mission. The satellite will attempt to downlink the collected data whenever it passes over the NASA Wallops ground station and is given instructions to begin downlink.

The majority of the time, the satellite will be in stand-by mode; in other words, it will not be capturing or downlinking data. In case of a subsystem malfunction, the satellite will go into safe mode to diagnose the source of the problem.

Analyses performed using STK predict that the satellite will deorbit within 7.8 years. This timeline agrees with the current 25-year deorbit requirement outlined by NASA standards.²

2.3 N^2 Diagram

In the early stages of the design process, the team created an N^2 diagram to exchange input and output values. Additionally, this diagram became an essential tool in determining the levels of interaction between the satellites different subsystems.

Payload	↘		↘	↘	↘	↘	↘
	Comm	↘	↘	↘	↘	↘	↘
	↗	Orbit	↘		↘	↘	
			Power	↘	↘	↘	↘
	↗		↗	ACDS	↘	↘	↘
	↗		↗		Avionics	↘	↘
			↗		↗	Thermal	↘
					↗	↗	Structures

Figure 2: High-Level N^2 diagram showing input/output relationships between subsystems

As highlighted the figure above, the payload requirements drive the design of all the other subsystems. While it does not receive design inputs from other subsystems, its design outputs cascade down effectively driving the design of the rest of the satellite.

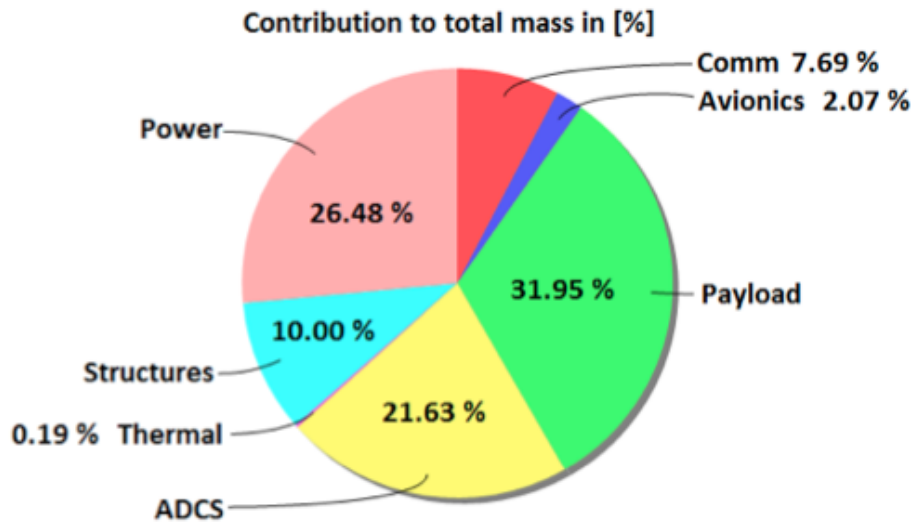
Feedback loops were present between several subsystems, which forced the team to perform trade studies to exchange performance for mass or power cost. One of these trades involved the design of the Power and ADCS subsystems. For example, complex solar panel

designs that could absorb more solar energy, such as deployable panels, would require a more robust ADCS subsystem. However, such ADCS design would need to draw more power to maintain the panels facing towards the sun effectively cancelling the power gained. After careful consideration of costs and benefits, the team decided to take this option off the table

2.4 System Level Budgets

2.4.1 Mass

The mass budget is presented in Figure 3 below.



2.4.2 Power

The power budget is presented in Figure 4 below.

3 Subsystems

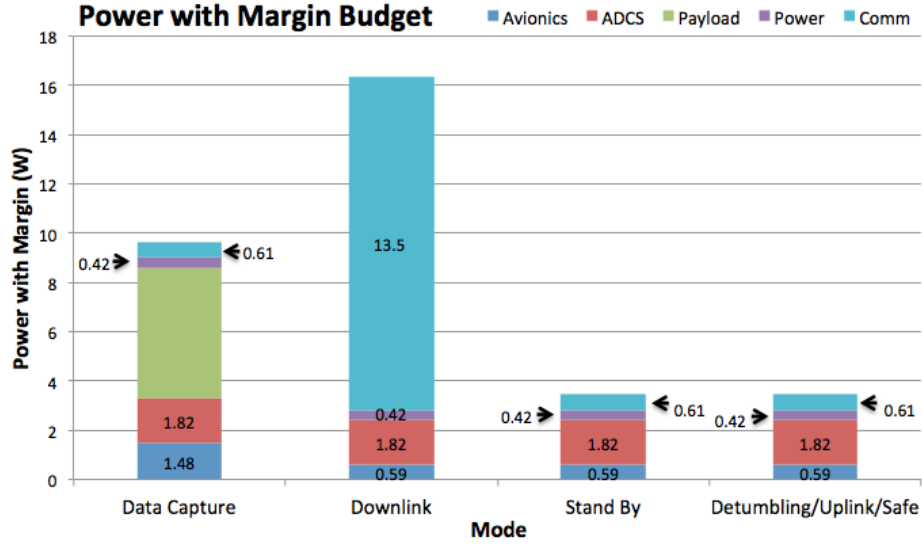
3.1 Payload

3.1.1 Requirements - AC

There are two types of payload requirements, the first set applies to the deformable mirror system. The second set pertains to the measurement and reconstruction of the wavefront. (All requirements are displayed in Appendix A.)

Mass Budget			
Subsystem	Mass Estimate (kg)	Margin ¹	Mass Budget (kg)
Structures	0.30	30%	0.39
Power	0.94	10%	1.03
ADCS	0.70	20%	0.84
Avionics	0.06	30%	0.08
Comm	0.25	20%	0.30
Payload	1.00	25%	1.25
Thermal	0.01	15%	0.01
Total	3.26	--	3.90

Figure 3: System Mass Budget



The deformable mirrors must operate for at least 5 minutes per orbit (PLD-1). This requirement comes from the mission level requirements (MLR-3, MLR-4) to characterize the deformable mirrors. The individual actuators that make up the deformable mirror must have a response time of less than or equal to 0.001 s, with a control rate of at least 100 Hz. The stroke must be at least 1.5 μm , with control precision of less than or equal to 1 nm.

The requirements on measuring and reconstructing the wavefront are requirements on the detector. Nominally, the detector must operate (take images) for at least 5 minutes per orbit, and be able to function at at least 10 Hz (PLD-2). The requirement is further separated

Power Budget			
Mode	Duration [min/day]	Power [W]	Power [W] (with 18 % Margin)
Safe/Uplink	--	2.92	3.44
Detumbling	~2 weeks	2.92	3.44
Data Capture	75	8.17	9.64
Downlink	46.7	13.84	16.33
Stand By	1318.3	2.92	3.44
Average	--	3.54	4.18
Power Supplied			3.84

Figure 4: System Power Budget

into a Diagnostic Mode, used for calibration and for full frame images, and a Burst Mode, used for data capture. Diagnostic Mode is required to take images for at least a minute per orbit at 10 Hz (PLD-2.1). Burst Mode is required to take images for at least 30 seconds per orbit at least 100 Hz (PLD-2.2). For both modes, the reconstruction accuracy must be less than or equal to 100 $nm\ rms$ (PLD-2.3).

3.1.2 Trade Studies and Decisions Made - AC and KB

Payload Architecture - AC While in future applications the deformable mirror will be used to aid in observing stars or other objects, the mission goal is to characterize the deformable mirrors in an easy platform, making the internal laser source desirable for this technology demonstration. There are many different techniques to measuring and reconstructing a wavefront [16]. Only sensed approaches are considered for this platform due to the compact form factor and desire for simple components. There are many wavefront sensing approaches that could be implemented, as well as improved or modified versions of those presented here, which could be considered in future analyses, but the two approaches discussed in detail are a Michelson Interferometer and a Shack-Hartmann Wavefront Sensor.

Michelson Interferometer with Linear Stager The interferometer design shown in Figure 5 is slightly modified from a typical interferometer due to volume constraints on the payload and the requirement for high contrast imaging. It has an internal source (laser diode), whose path is denoted by a dotted red line. The laser beam is first resized, then is reflected 90 degrees by a flat mirror. The light is then divided by a beam splitter oriented 45 degrees to the beam. The transmitted beam travels to the deformable mirror where it is

reflected back towards the beam splitter. Half of the beam is deflected by 90 degrees at the beam splitter and strikes the detector. The reflected beam travels to the flat mirror on the linear stager where it is reflected and half of it then is transmitted through the beam splitter and reaches the detector. The two beams that reach the detector interfere to produce fringes that are analytically well understood as a function of beam coherence/divergence and mirror tip/tilt [8] and that can be simulated for a variety of different deformable mirror shapes.

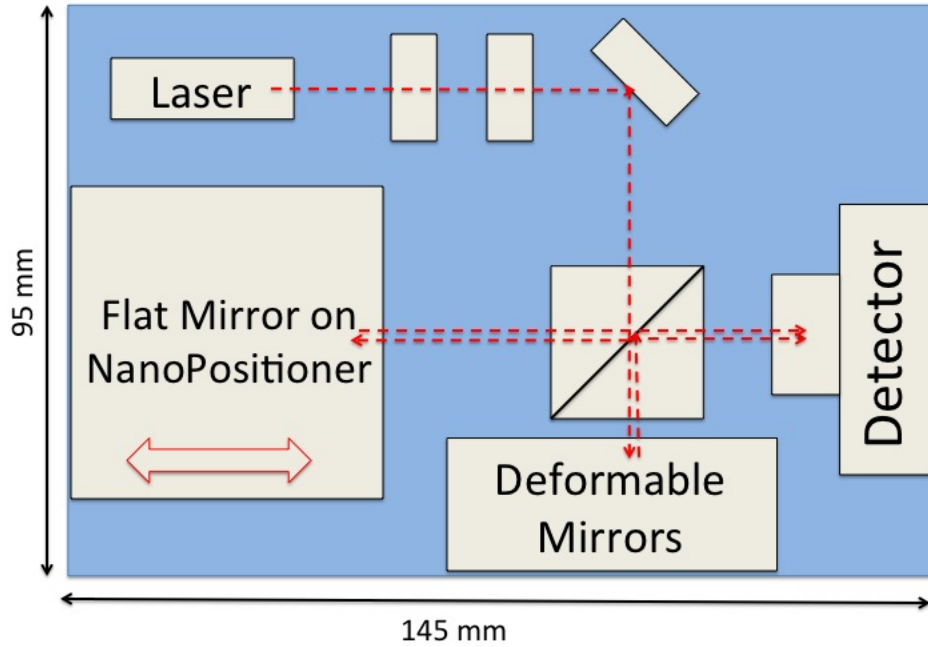


Figure 5: This is the Michelson Interferometer with the flat mirror on a linear stager. This is a payload design possibility.

For this particular design, as mentioned previously, a flat mirror is on a piezo linear stager which moves in increments of fractions of the incoming wavelength. This allows for higher precision fringe patterns (reference?), allowing for better mirror characterization.

What is not shown in Figure 5 is the controller for the linear stager. It does not currently fit within the constraints of the satellite in terms of mass, volume, and power needs. It would require significant modifications, if it were to be implemented. Also, the additional moving part increases the risk and complexity of the mission.

Shack-Hartmann Wavefront Sensing System For the wavefront sensing design in Figure 6, a Shack-Hartmann lenslet array on the detector is used, allowing for accurate

wavefront measurement and reconstruction sensitivity. The design has an internal source (laser diode), whose path is denoted by a dotted red line, and an aperture for imaging an external source, whose path is denoted by a dotted green line.

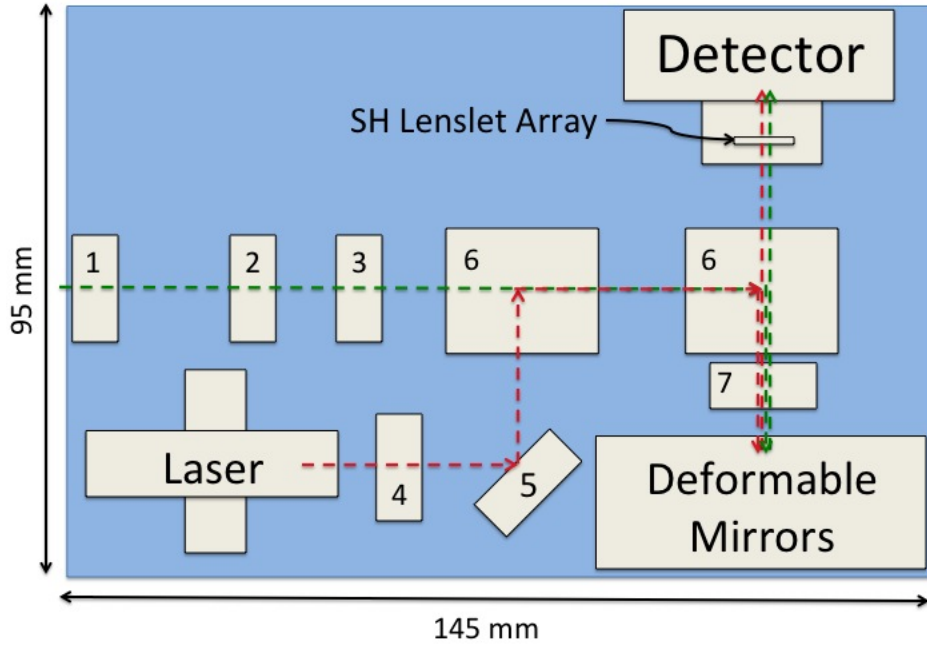


Figure 6: This is the Wavefront Sensing design with a Shack-Hartmann lenslet array. This is a payload design possibility.

For the internal source, the laser diode module emits a collimated elliptical beam. This beam enters a linear polarizer (where its intensity is halved). The beam then encounters a flat mirror at 45 degrees, reflecting the beam 90 degrees, and proceeds to a primary beam splitter. Here, the beam is reflected 90 degrees to secondary polarizing beamsplitter, and reflected another 90 degrees. The beam then goes through a quarter waveplate (where the beam is now elliptically polarized) before striking the deformable mirrors. The deformable mirrors reflect the beam back through the quarter waveplate, rendering the beam now linearly polarized with an orientation that allows it to pass through the secondary beam splitter. The beam then proceeds through the microlenslet array, creating a spot diagram on the detector corresponding to shape of the wavefront.

For the external source, the wavefront beam enters a plano-convex lens and then passes through a collimating lens. The beam then enters a linear polarizer (where the intensity is halved). The beam then passes through the primary beam splitter, and then to the secondary

polarizing beamsplitter, which reflects the beam 90 degrees towards the quarter waveplate and the deformable mirrors, as mentioned previously, and follows an identical path to the detector.

Design Decision The mission goal is to characterize the deformable mirror system, and to accomplish this with COTS as much as possible to allow for a quick and easy platform for space (MLR-3, MLR-4). While the interferometer with the linear stager is able to achieve higher precision, the Shack-Hartmann wavefront sensing system will fit with minor modifications to components, and allows for sufficient mirror characterization, meeting our mission goal and requirements. Therefore, the Shack-Hartmann wavefront sensing design in Figure 6 has been chosen to image the wavefront.

The chosen design allows the detector to image both an internal and external source. While the mission goal can be accomplished with just an internal source, the ultimate goal of using this technology on a larger space telescope for imaging of bright stars motivates the use of an external source. Therefore, the option for an external source will be included in the design.

Due to the added complexity required of the ADCS system on a CubeSat platform, the external source imaging will not require knowledge of particular stars and navigating there. In contrast, with pointing knowledge from ADCS, the shutter on the aperture will be commanded open when a bright star is in the field of view (FOV). Additional work is needed to evaluate revisit times to particular stars. Pointing requirements on the maximum ADCS slew rate to keep the star on the same pixels on the detector are discussed in Section ??.

The aperture for imaging an external source will necessarily be small, given the volume constraints of the CubeSat platform after accommodating all of the key elements of the system (deformable mirror, mirror driver electronics, detector, and necessary imaging optics). Due to these key elements, it is not practical to design the external source imaging as a reflecting telescope. While it may be possible to accommodate a larger aperture lens ($> 60\text{ mm}$), the corresponding longer focal length would not fit in the space, and the space for resizing the beam is limited. While the smaller aperture will limit the angular resolution and sensitivity and increase the size of the point spread function (PSF), tight angular resolution is not a requirement for this technology demonstration. Therefore, an aperture lens with diameter 12.7 mm has been chosen, with a minimum focal length on the order of its diameter. Using the Rayleigh criterion, the angular resolution (width of the center of the PSF) at 500 nm would be $2.436''$ (NEED TO CHECK number, because I'm getting double this.).

The current design is an open loop system, where images and centroid solutions (reference to how centroids are found?) are sent to the ground, and analyzed there. Then, commands can be sent to the payload about how to correct the wavefront. However, the choice of a Shack-Hartmann design makes it easier to incorporate closed loop control for future follow up missions. The option of active correction of the wavefront on-orbit with the current design can be accomplished by the addition of a few components and requiring more on-orbit processing.

All optical elements of the system have been preliminarily chosen. See Appendix ?? for the full list of elements with part numbers and mass totals. Glass elements were chosen to be UV fused silica over other glasses whenever possible for their better performance in space [13] due to a high coefficient of thermal expansion and better UV transmission. All elements also have anti-reflective coatings that are efficient in the visible spectrum (400 - 700 *nm*). Mounts have been chosen for all components, however, these are only estimates of the custom mounts that will be built for all optics. The reason for this is due to the space application. All elements must be mounted in stress-free mounts (no glass touching metal, etc.) and mounted to an optical breadboard with multi-footed lens tubes that are made of aluminum, or of a metal that has the same coefficient of thermal expansion as the lenses they hold. Future modeling and optimization of the optical design will yield more exact component choices.

Payload Operations For the initial demonstration and on-orbit testing, we will use an internal light source. This eliminates any payload specific requirements on the satellite's attitude and inclination. For the latter half of the mission, we will use an external light source, attempting to image the optical wavefront from a star.

After detumbling, and thirty days of commissioning, as describe in Section ???, the payload will perform a status check of all instruments. This includes the deformable mirror system, the detector, and the laser. Each element will be turned on and checked for any error or status codes. Then, the payload will take some TBD sequence of test images, with TBD sequence of mirror positions (not very many, not very frequently). The full-frame images will be sent down with centroid solutions and any available status information directly from the deformable mirrors and the detector.

The next phase is to calibrate the system. This involves turning on the laser and recording several images in this configuration with the detector, without deforming the mirrors (acts as a flat mirror). From these images, one can find the centroids and average them to obtain new

'standard centroids' which will be used for wavefront comparison calculations throughout the remainder of the mission. These images, averages, and new centroid solutions will be sent to the ground.

The next, and primary, stage is data capture using the internal source. The laser is turned on, then the mirror is deformed by a predetermined test sequence of commands, and the wavefront is imaged on the detector. The test sequence will include 'poking' one actuator at a time, and 'poking' combinations of actuators. Then, the images are read from the detector, centroids are found, and one full image and the collection of centroid solutions are sent down to the ground.

The second part of data capture will be with an external source. With knowledge from ADCS, the shutter will be commanded open, and the laser will be commanded off, allowing some TBD external source to be imaged. The images are read from the detector, the centroids are found, and one full frame image along with the collection of centroid solutions are sent to the ground. All downlinked files are timestamped.

Deformable Mirror System - KB

Detector - KB

Shack-Hartmann Lenslet Array - AC A Shack-Hartmann lenslet array consists of an array of lenses (called lenslets) of the same focal length, where the array is focused on the detector. Each lens creates a spot, creating a spot diagram on the detector. Figure 7 demonstrates incoming light through a lenslet array. The local tilt of the wavefront across each lens can then be calculated from the position of the focal spot on the sensor; the displacement, Δx , equals the local slope of the wavefront. Any phase aberration can be approximated to a set of discrete tilts. By sampling an array of lenslets all of these tilts can be measured and the whole wavefront approximated. One thing to note: since only tilts are measured, the lenslet array cannot detect discontinuous steps in the wavefront.

To get the best measurement of the wavefront, the maximum number of spots, and therefore lenses, is desired. As a result, for a constant beam size, a lenslet array should be chosen with the lowest pitch (distance from the center of each lens) in order to get the maximum number of spots for the beam.

Therefore, MLA150 (Figure 8) was chosen from ThorLabs, with a pitch of $150\ \mu m$. The lenslet is $10\ mm^2$ square, so it contains about 66 by 66 microlenses. It has a $9\ mm^2$ square effective aperture, with a focal length of $5.2\ mm$, and will be mounted in the lens tube on the

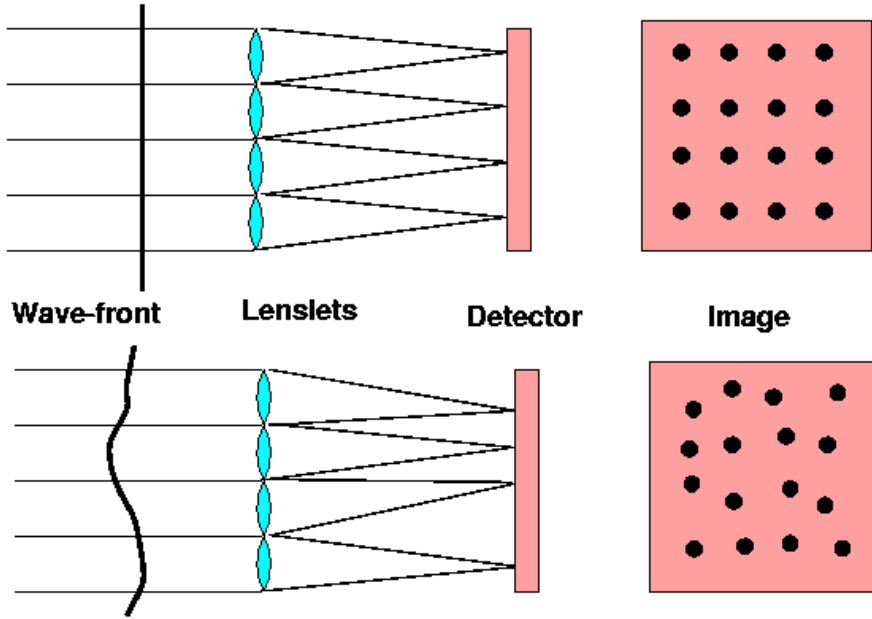


Figure 7: This figure demonstrates the result of two wavefronts, plane and aberrated, entering a Shack-Hartmann lenslet array, and their resulting spot diagrams on the detector.

detector (see Paragraph ??). For an approximate beam size of 2.25 mm (see Paragraph ??), approximately 15 by 15 lenses will be used of the lenslet array. As discussed in Paragraph ??, a 2.25 mm incoming beam corresponds to about 425 px^2 square, allowing for over 20 pixels per spot, so there is no concern for multiple spots falling on the same pixel.

3.1.3 Analysis

3.1.4 Summary of Outputs - AC

The payload's operational requirements are major drivers for the design of the rest of the satellite. A summary of mass totals, power needs, and thermal requirements of all major Payload components can be found in Table 1. During data capture mode, the payload needs to be kept within 0°C to 50°C , will draw a maximum power of 4.5 W , will output a maximum data rate of 550 Mbit/s , and, during external data acquisition only, has a maximum slew rate of $4.7'/s$. With all components, the Payload is about 997 g , or 1.25 kg with a 25% margin.

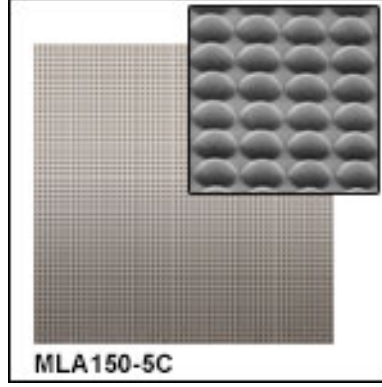


Figure 8: This is the MLA150 lenslet array from ThorLabs choosen for the Shack-Hartmann Wavefront Sensing design.

Table 1: This is a summary of the mass totals, power needs, and thermal needs of the major payload components.

Component	Mass (g)	Power (W)	Thermal, operating ($^{\circ}\text{C}$)	Thermal, storage ($^{\circ}\text{C}$)
Laser diode	24.45	0.0045	-10 to 50	unknown
Detector	46.64	$< 2\text{ W}$	0 to 50	-20 to 80
Def. Mirrors + Driver	189.9	$< 2.5\text{ W}$	-10 to 50	unknown
Optical Breadboard	~ 250			
Optical Enclosure	~ 300			
Totals	996.9	4.5 W max	0 to 50	-20 to 80

3.1.5 Requirements

3.1.6 Trade Studies and Decisions Made

Deformable Mirror System - KB

Detector - KB

3.1.7 Analysis

Pointing Requirement - KB

3.1.8 Summary of Outputs

3.1.9 Risks

3.1.10 Future Work - AC

- Optical Modeling in ZEMAX: Determine final beam profile on the detector, Optimization of space to find the best choice of components, Explore thermal effects on beam and optical components
- Interferometer with Linear Stager Design Feasibility: Can nanopositioner elements be scaled down for a CubeSat platform?, What would the effects be on other subsystems?
- Imaging External Sources: Need to determine when and how to image an external source (FOV, star sensors)
- Closed Loop Control: Determine difficulty in implementation
- Stroke Analysis: Study properties of DM stroke

3.2 Power - JC

3.2.1 Requirements

The Power subsystem is required to supply power to all other subsystems under all conditions. In particular, it must supply an average of 3.54 watts on average over the course of the orbit (calculated in Section 3.2.4, Analysis), sustain a maximum load of 13.84 watts during certain operational modes (downlink mode, per Systems), have a minimum battery capacity of 3.9 watt-hours (calculated in Section 3.2.4, Analysis), and meet these requirements for up to 1 year, or approximately 6,000 cycles (calculated in Section 3.2.4, Analysis).

3.2.2 Trade Studies and Decisions Made

Using STK, we compared the average power obtained by the solar panels under several circumstances. The two variables were the inclusion or omission of a solar panel on the top face of the satellite, in addition to the four side-mounted panels, and the orientation of the satellite in its orbit – whether it flew “face-first”, with the normal vector of one of its sides aligned with its velocity, “corner-first”, where it is tilted by 45 degrees about its long axis from the face-first orientation, or spinning about its long axis. The face-first and corner-first attitudes are illustrated below:

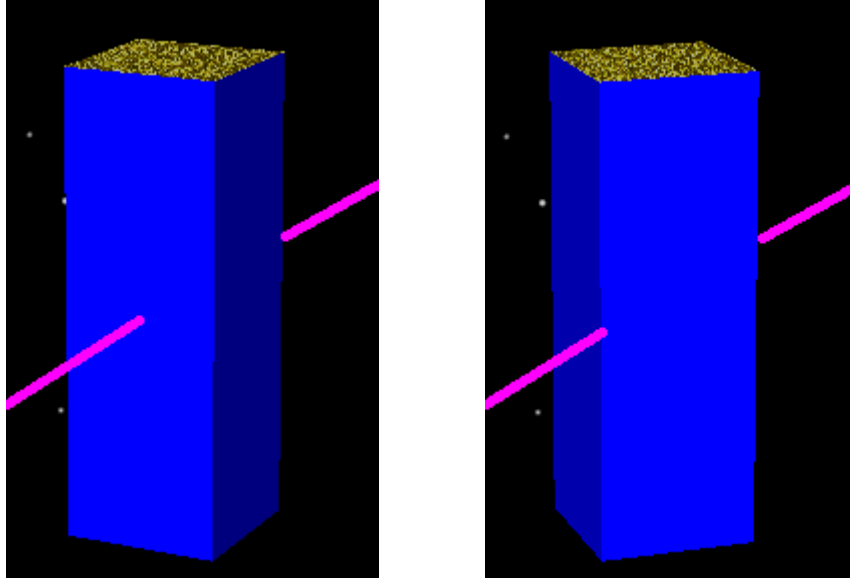


Figure 9: The “face-first” and “corner-first” attitudes. Images generated from STK.

Table 2: Power values for various panel configurations and satellite attitudes.

	Face-first	Spinning	Corner-first
Side panels	3.77 W	4.16 W	4.52 W
Side and top panels	4.45 W	4.84 W	5.19 W

Note that these power values are averaged over the entire orbit – that is, taking the incoming power to be zero during local night and including that in the average. This was done because the satellite is active during the entire orbit, and its average power needs are calculated over the entire orbit; to ensure that we are comparing likes against likes, we did the same for the power generated.

3.2.3 Decisions Made

In general, the power subsystem was designed to be as simple as possible while meeting the satellite’s power needs. We chose to use stock parts as much as possible because they have known performance, which helps us verify that requirements are met and reduces the margins we need to hold.

The chosen solar panel configuration was four body-mounted side panels. Body-mounted panels were chosen over deployable panels because they minimized the surface area of the



Figure 10: The solar panel configuration to be used on the DeMi satellite. Image from Clyde Space.[1]

satellite, which minimized the disturbance torques, and they are symmetrical, reducing the pointing constraints on the ADCS. The satellite would be oriented in a nadir-pointing configuration, so the nadir face would almost never see any sunlight, so we chose not to panel it, and we chose not to panel the zenith face to allow the payload to have an aperture in that face, so that it could potentially image external light sources.

The remainder of the power system is similar to that of most other satellites: an electrical power system module takes power from the solar panels and manages the current and voltage levels to ensure that the panels deliver power at maximum efficiency, a secondary (rechargeable) battery supplies the satellite with energy during eclipse, and a power distribution module supplies power to systems which are not part of the main system stack, like the torque coils.

The satellite's power subsystem does not include a primary battery. A primary battery was never included in the design because the satellite was to be covered on most sides by solar panels and would be power-positive in detumbling mode, so it would charge as soon as it exited the P-POD. The only reference to a Cubesat containing a primary battery was a description of a Cubesat that lacked solar panels entirely.[2]

3.2.4 Analysis

The average power required is the time-weighted average of the power required during the various modes of the satellite:

$$P_{req,avg} = \frac{1}{T_{total}} \sum_{modes} \sum_{systems} T_{mode} P_{sys,mode} = 3.54 \text{ W} \quad (1)$$

The solar panels are required to gather enough power during the day to power the satellite for the entire orbit, when taking the inefficiency of the EPS into account ($\eta = 0.85$ in the worst case[3]):

$$P_{req,panels} = \frac{T_d + T_e}{T_d} \frac{P_{req,avg}}{\eta} = 6.61 \text{ W (cold)}, 5.21 \text{ W (hot)}, 4.16 \text{ W (orbit avg)} \quad (2)$$

“Hot” and “cold”¹ here refer to the two orbital cases which have the most and least solar exposure for the satellite because the orbit is fixed in inertial space, it appears to rotate with respect to the Earth-Sun vector over the course of a year. Every six months, it goes from a cold orbit, which is in the sunlight 63% of the time, to a hot orbit, which is 80% sunlit, and back again. The two orbits are illustrated below.

The satellite drains the most energy from the battery if it performs a ground station pass (maximum duration: 9.77 minutes, per Comm) and scientific operation (nominal duration: 5 minutes, per Payload) during local night:

$$E_{req,batt} = T_{sci}P_{sci} + T_{comm}P_{comm} + (T_e - T_{sci} - T_{comm})P_{standby} = 3.9 \text{ Wh} \quad (3)$$

The excess power is the power actually generated by the panels that does not go into powering the satellite or charging the battery – in other words, the difference between the power required power and the power actually generated:

$$P_{excess} = P_{panels} - P_{req,panels} = 0.63 \text{ W (cold)}, 2.57 \text{ W (hot)} \quad (4)$$

It can be useful to model the excess power as an average over the entire orbit, rather than just happening during local day (for first-order approximations of the equilibrium satellite temperature):

$$P_{excess,avg} = P_{excess} \frac{T_d}{T_d + T_e} = 0.40 \text{ W (cold)}, 2.06 \text{ W (hot)} \quad (5)$$

The number of charge-discharge cycles of the battery is approximately equal to the num-

¹Perhaps “bright” and “dark” would be better terms from a power perspective, because it is not temperature that gives us power but sunlight.

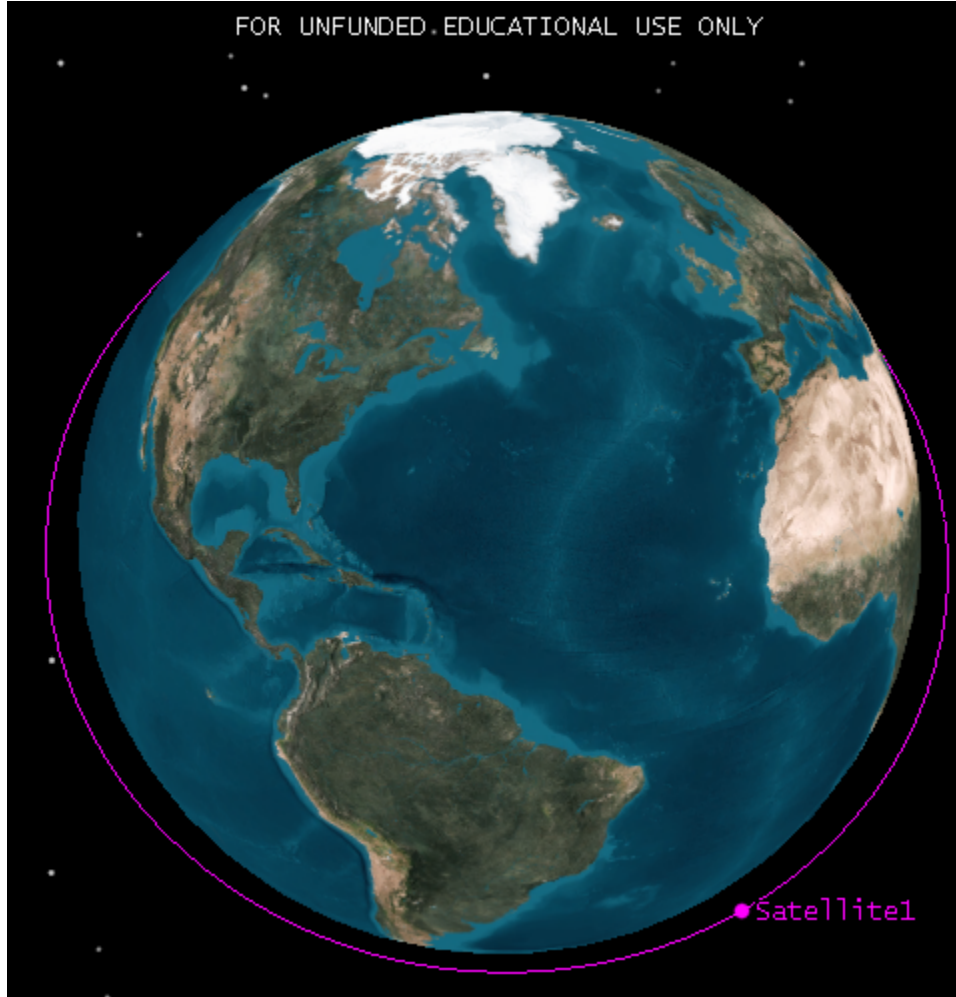


Figure 11: A “hot” orbit, where the satellite is exposed to the sun 80% of the time. Image generated from STK.

ber of orbits that the satellite will have to sustain:

$$N_{cycles} = \frac{T_{year}}{T_{orbit}} = 5500 \approx 6000 \text{ (with 10\% margin)} \quad (6)$$

3.2.5 Summary of Outputs

The solar panels do not literally have zero volume, but because they are fixed to the sides of the Cubesat, they do not occupy any of the three units of internal volume.

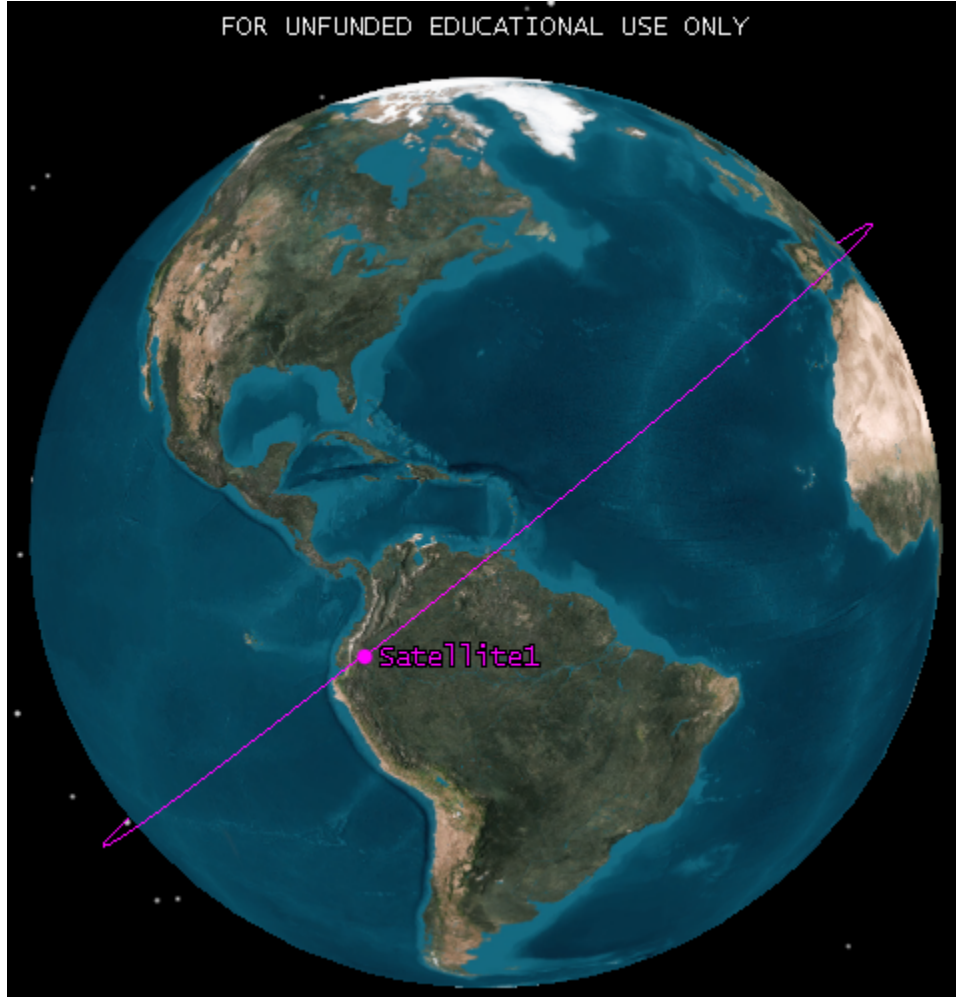


Figure 12: A “cold” orbit, where the satellite is exposed to the sun 63% of the time. Image generated from STK.

3.2.6 Risks

The primary risk facing the Power subsystem is that our incoming power is fundamentally limited, so we will have to be careful to not exceed our budget. As computed in Analysis (Section 3.2.4), the average power drawn by the satellite for nominal mode durations is 3.54 watts. While the orbit-averaged power coming in from the solar panels is 4.52 watts, which is a 28% margin over the power needs, when we take the worst-case efficiency of the EPS’s solar-panel connection into account[3], we find that as little as 3.84 watts are actually getting to the battery power bus, leaving only a 9% margin (which might then be further eroded by inefficiencies in the power lines). This is less than the 18% margin goal we had set for ourselves, and substantially less than the 30% margin that JPL informed us was their usual

Table 3: Outputs to other systems (mass, volume, power consumed, and survival and operating temperatures).[3] [4] [5] [6]

Component	Mass (kg)	Volume (U)	Power consumed (W)	Survival temperature (° C)	Operating temperature (° C)
Solar panels	0.540	0	0	-40 to 80	-40 to 80
EPS	0.083	0.15	0.1	-50 to 100	-40 to 85
Battery	0.256	0.2	0.1	-10 to 50	0 to 50
PDM	0.060	0.25	0.16	-50 to 100	-40 to 85
Total	0.939	0.6	0.36	N/A	N/A

standard for satellite missions.

This risk is mitigated by the 32% margin of available power over the standby power need of 2.91 watts. From this, we can be confident that, even in the worst possible case, the satellite will be power-positive during its standby mode. This means that, if the satellite should find itself unable to meet its power needs for nominal mode durations, it could be commanded to spend more time in standby mode and less in data capture or downlink mode to restore balance to its power budget. As mentioned in the Analysis section, the available power was calculated for the coldest, darkest orbit that the satellite will be in. For the brightest orbit, the average power generated by the solar panels over the entire orbit increases to 7.42 watts, which, taking the worst-case EPS efficiency into account, results in 6.31 watts reaching the power line, which is a 78% margin over the average power required. In fact, we could spend 29 minutes – nearly six times the nominal data capture mode duration – of such a bright orbit in data capture mode (leaving the downlink mode duration constant, as ground pass durations are independent of available power) while maintaining a 30% margin of available (post-EPS) power over required power. We can thus be assured that, even if the satellite is forced to reduce the duration of data capture and downlink modes during darker orbits to conserve power, we can make up for any shortfalls of captured data during better orbits.

3.2.7 Future Work

The performance of the solar panels and batteries is temperature-dependent. In particular, the battery becomes more effective as its temperature increases, while the solar panels become less so. Going forward, it would be useful to perform a more detailed simulation of the satellite that incorporates a thermal model, so that we can more accurately measure the

effect of satellite temperature and dissipated excess energy (energy from the solar panels that does not go into charging the battery or powering the satellite).

3.3 Communication

3.3.1 Requirements - ZC

Most of the Communications requirements (see Appendix A) are standard Communications requirements for operability. Comm-1 is simply stating what the main goal of the Communications subsystem is. Comm-2 is there to ensure that the link with the ground station is good enough to transmit all of the data that we need to. Comm-2.1 is there so that if there is an error in the transmission, the system will be able to realize this and ask for a correction. Comm-2.2 is so that it doesn't try to downlink more data than possible because if it does, then data will be lost. Comm-3 is simply there so that the Communications subsystem can ensure access with the ground station. Comm-3.1 and Comm-3.2 are specifics when it comes to communicating with the ground station. Comm-4 is there because if we do not encrypt it, another satellite may be able to receive our commands and learn about the DeMi system. Comm-5 is there to ensure that if there are errors, there will be very few of them. Comm-6 is just to ensure that DeMi follows all regulations set by different government agencies.

3.3.2 Trade Studies - ZC

The main factor in choosing what transceiver to use in our system is the data downlink amount. Because payload is generating so much data, Communications will need to have a high downlink rate to ensure that all of that data can be sent to the ground. Several options were looked into, and shown in Table 4.

Table 4: Communications Trade Study for Maximum Downlink Data Rate

Tranceiver	Maximum Downlink Rate
Espace Payload Telemetry System	1 <i>Mb/s</i>
AstroDev Li-1 UHF Transceiver	38.4 <i>kb/s</i>
ISIS TXS Small Satellite S-Band Transmitter	100 <i>kb/s</i>
Tyvak UHF Transceiver	200 <i>kb/s</i>
L-3 Cadet Nanosat UHF Radio	1.5 <i>Mb/s</i>
Microhard MHX2420 Modem	230.4 <i>kb/s</i>

3.3.3 Decisions Made - ZC

Given the information in Section 3.3.2, the L-3 Cadet Nanosat UHF Radio was chosen for use on DeMi. It will transmit at the frequencies and data rates outlined in the requirements, which are 445 – 455 MHz for uplink at 19.2 kb/s , 460 – 470 MHz for downlink at 1.5 Mb/s . The transceiver also has an extra 4 GB of storage that avionics will be able to use in addition to any of its storage.

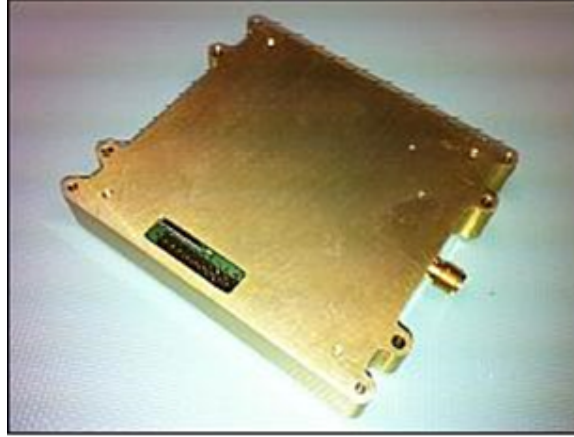


Figure 13: Photo of the custom-designed high-speed L3 Cadet radio [9].

Because the transceiver will be transmitting and receiving at UHF frequencies, a very common antenna choice is to use a measuring tape antenna that is tuned to the frequency that is desired. Because the antenna works like a quarter-wave monopole, one can determine the desired length of the antenna by dividing the wavelength of the transmitted and received signal by 4. Because the transmitting and receiving frequencies are different, the average of these frequencies was used to compute the wavelength.

$$\lambda = c/f \quad (7)$$

Eq. 7 is used to calculate the wavelength. λ is the wavelength, c is the speed of light, and f is the frequency. Using the average frequency of 465 MHz , the wavelength equals 0.645 m . Then to determine the length of the antenna one can just use the following equation.

$$l = \lambda/4 \quad (8)$$

In Eq. 8, l is the length of the antenna, and λ is the wavelength. Using a wavelength of 0.645 m , one can find that the desired length of the antenna is about 0.164 m . The gain of

this antenna will be approximately 3 dB and the beam width approximately 65° .



Figure 14: Photo of stored and deployed measuring tape antenna. The pictured CubeSat has four antennas. DeMi will only be using one [11].

The ground station that will be used with this system will be the NASA Wallops UHF Ground Station. This was chosen because the transceiver that will be used was also used in the Dynamic Ionosphere CubeSat Experiment, and the ground station that was used in that mission was the NASA Wallops UHF Ground Station. The diameter of the dish is 18.29 m , the gain is 35 dB and the beam width is 2.9° .

3.3.4 Analysis - ZC

One can calculate the maximum amount of data downlink per pass-by by multiplying the downlink data rate and the access duration per pass-by. Given the downlink data rate of 1.5 Mb/s , and the access duration of 586 s per pass-by, the maximum amount of data that can be downlinked in one pass-by is 109.9 MB . To account for the fact that the data-rate won't always be able to be at its maximum, and also for space for telemetry data and error correcting code, we have a margin of a factor of 2, so the maximum amount of data from payload that can be downlinked per pass-by is about 54.95 MB . Although this is not as much data as payload is creating, there will be on-board processing so that the amount of data that needs to be downlinked is below the maximum amount that is allotted for payload.

A Link Budget was created in order to determine the Link Margin for a worst case and a best case for uplink and downlink. Appendix B detail these budgets.

The first calculation in the Appendix B is to calculate the worst case propagation path length. We know that the best case length is 500 *km* because that is the altitude at which the satellite is orbiting. Figure 15 shows how a wave propagates through that atmosphere and will be explained beneath.

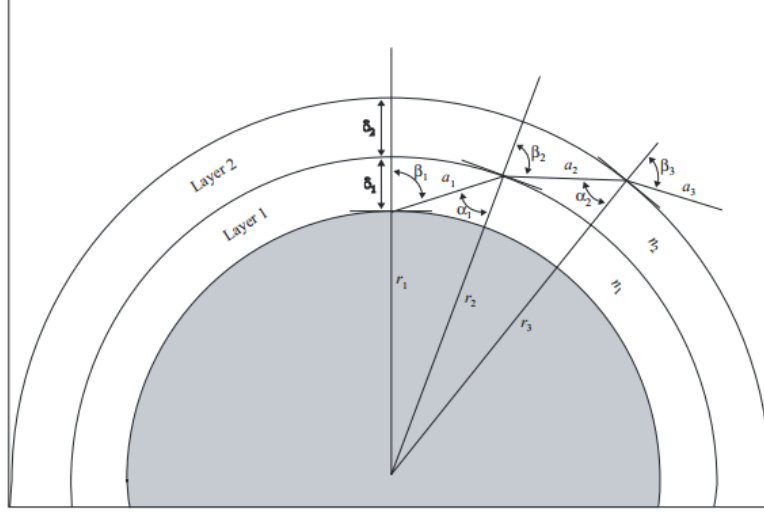


Figure 15: Diagram of propagation path of a signal from a satellite [12].

In order to determine the propagation path length, r , one must determine the path length of the first layer and the second layer and add them together. The equation for calculating [12] the path length of a layer is as follows.

$$a_n = -r_n \cos(\beta_n) + \frac{1}{2} \sqrt{4r_n^2 \cos^2(\beta_n) + 8r_n \delta_n + 4\delta_n^2} \quad (9)$$

In Eq. 9, a_n is the path length through layer n , r_n is the radii from the center of the Earth to the beginning of layer n , β_n is the exiting incidence angle, and δ_n is the thickness of layer n . The angle β_n can be calculated [12] using the following equation.

$$\beta_{n+1} = \arcsin\left(\frac{n_n}{n_{n+1}} \sin(a_n)\right) \quad (10)$$

In Eq. 10, n_n is the refractive index of layer n , and α_n is the entry incidence angle. Angle α_n can be calculated with the last equation needed in order to calculate [12] the propagation length.

$$a_n = \pi - \arccos\left(\frac{-a_n^2 - 2r_n \delta_n - \delta_n^2}{2a_n r_n + 2a_n \delta_n}\right) \quad (11)$$

Values that still need to be defined are β_1 (because it cannot be calculated using Eq. 11), δ_1 , δ_2 , n_1 , and n_2 . β_1 is just equal to the complimentary angle to the minimum angle at which the Wallops Ground Station can track, which is 5° . δ_1 will be equal to the altitude at which the atmosphere ends which one can say is about 100 km . δ_2 is just the orbiting altitude minus δ_1 . n_1 , which is simple the refractive index of air, is 1.000293. The last remaining value to be defined is n_2 , which is the refractive index of a vacuum, which is just 1. Using these equations, one can find that a_1 equals 707 km , and a_2 equals 1375 km . This means that the worst case propagation path length is equal to 2082 km .

The next value calculated in the Link Budgets is the Equivalent, Isotropic Radiated Power (EIRP). In order to calculate the EIRP [17], the following equation should be used.

$$EIRP = P_{tx} + G_{tx} - L_{output} \quad (12)$$

In Eq. 12, P_{tx} is the transmitter power, G_{tx} is the transmit antenna gain, and L_{output} is the output loss which is equal to all losses associated with the transmitter. All of these values can be found in the Link Budget (Appendix B).

Another calculated value in the Link Budget is the Space Loss. This is the loss of the signal as it is transmitted through space. It can be calculated [17] using the following equation.

$$L_s = 92.45 + 20 \log_{10}(r) + 20 \log_{10}(f) \quad (13)$$

In Eq. 13, L_s is space loss, r is the propagation path length, and f is the frequency of the transmitted signal. All of these values can also be found in the Link Budget (Appendix B).

The next equation can be used to calculate [14] the transmitting antenna temperature.

$$T_{antenna} = \eta T_{sky} + (1 + \eta) \frac{T_{sky} + T_{ground}}{2} \quad (14)$$

In Eq. 14, η is the antenna efficiency, T_{sky} is the temperature of the space behind the receiving antenna. The temperatures used for uplink are determined by using the background temperature of space. For downlink, the temperature of the Earth is used. T_{ground} is the temperature of the ground around the antenna. For uplink, this is the temperature of the Earth, and for Downlink, it is the background temperature of space.

The system noise temperature, T_{sys} , is calculated by adding the transmitting antenna temperature and the receiver temperature [14]. The receiver temperature for both cases is unique to the receiver and can be determined by the manufacturer.

The next calculated value is the Receiver Gain to Noise Temperature. This is computed [17] using the following equation.

$$\frac{G}{T} = G_{rx} - T_{sys} \quad (15)$$

In Eq. 15, $\frac{G}{T}$ is the Receiver Gain to Noise Temperature, G_{rx} is the receiving antenna gain, and T_{sys} is the system noise temperature. Using $\frac{G}{T}$, the total losses in the system, and EIRP one can determine [17] the Receiver Carrier to Noise Ratio.

$$\frac{C}{N_0} = EIRP + \frac{G}{T} - L_{total} + 228.6 \quad (16)$$

Using that value and the data rate in decibels, one can calculate [17] the Energy per bit to Noise Ratio.

$$\frac{E_b}{N_0} = \frac{C}{N_0} - R_b \quad (17)$$

Finally, the link margin can be determined by subtracting the required Energy per bit to Noise Ratio from the predicted one.

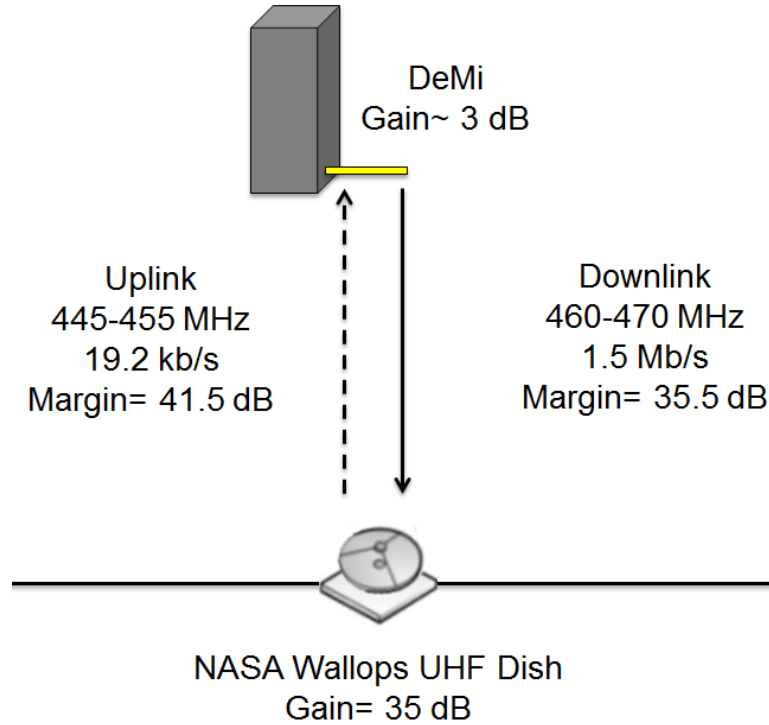


Figure 16: Representation of Satellite and Ground Station during Best Case Communication.

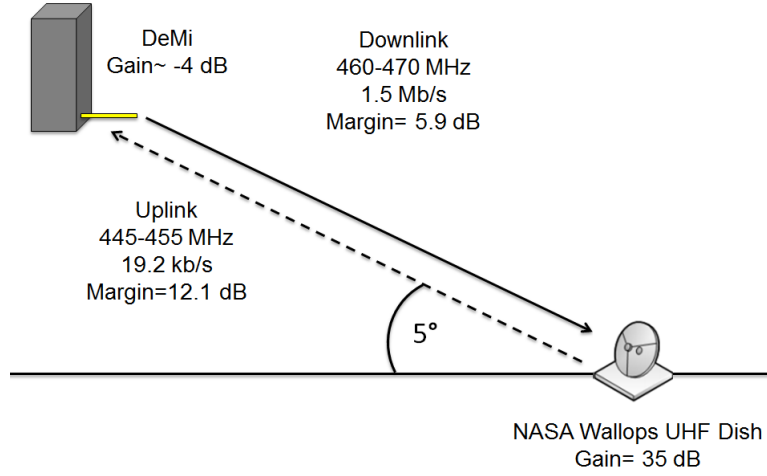


Figure 17: Representation of Satellite and Ground Station during Worst Case Communication.

3.3.5 Summary of Outputs - ZC

There were several outputs during the design process from the Communications subsystem. These outputs include the Ground station to Orbits, which is NASA Wallops UHF Ground Station, the beam width of Wallops UHF Ground Station and DeMi to ADCS, which are 2.9° and 65° respectively, the operational and survival temperatures of the transceiver to Thermal, which are -20°C to 70°C and -40°C to 80°C respectively. The power for each mode to Power, and the mass and volume to Structures are detailed in Table 5

Table 5: Communications Budgets

Output	Value
Power (Standby)	0.51 <i>W</i>
Power (Data Capture)	0.51 <i>W</i>
Power (Downlink)	11.44 <i>W</i>
Power (Uplink)	0.51 <i>W</i>
Power (Safe Mode)	0.51 <i>W</i>
Mass	0.235 <i>kg</i>
Volume	0.069 <i>U</i>

3.3.6 Risks - ZC

As of PDR, there were no risks for the Communications subsystem. Towards the beginning of the design process, there were huge concerns about Communications not being able to downlink enough of the data from Payload, but since then, Avionics has decided that DeMi will be doing on-board processing so that all of the data does not need to be downlinked.

3.3.7 Future Work - ZC

Moving on from here, the main thing that should be done is research and analysis of measuring tape antennas. There is currently not very much information out there that is available to DeMi concerning them, so research to determine the exact gain, beam width and radiation patterns should be conducted.

3.4 Avionics

3.4.1 Requirements - VE

The Avionics subsystem requirements are presented in Appendix A. The main driving requirements are number 3 and 2 in the order of importance because they are the most challenging to satisfy with a current level of technology.

3.4.2 Trade Studies - VE

We have two main options that are able to satisfy the requirements for Avionics subsystem. Both are shown in Table 6

Since we have identified the Payload driven requirements as the most challenging, we have to start selection of appropriate hardware from that.

Lets consider approach when we downlink all the data generated by the Payload without processing it. From Table 7 we can see that Payload will be generating around 1 *GB* of data every time it is run. For a given 1.5 *Mbit/s* downlink speed in this case we will need 600 *s* to downlink all the data captured or 10 ground accesses. Since we have only one ground access every three orbits in general this particular approach seems to be too ineffective in terms of Payload active time.

Thats why we mainly consider the second approach when we do all necessary calculations onboard and send only results to the ground. It dramatically reduces the amount of

Table 6: Hardware Options

	Processing on-board	Raw images to the ground
Component Name	The Steepest Ascent Mission Interface Computer CS-MIC-G-EM	Single Board Computer Motherboard + PPM with TI MSP430F2618
Power Consumption	0.5 – 1.25 W	10 mW
Capabilities	Telemetry/Telecommand + Real time image processing on FPGA	Telemetry/Telecommand
Storage Capacity	Up to 16 GB	Up to 2 GB
Processors	TI MSP430 + Xilinx FPGA (model can be selected)	TI MSP430F2618
Interfaces	I2C, SPI, UART	I2C, SPI, UART
Mass	62 g	88 – 114 g

Table 7: Payload image capturing modes

Mode	640x480 px subframe	640x480 px subframe	1280x1024 px full frame
Frame Rate	100 <i>fps</i>	10 <i>fps</i>	10 <i>fps</i>
Data Rate	310 <i>Mbit/s</i>	31 <i>Mbit/s</i>	131 <i>Mbit/s</i>
Duration	30 <i>s</i>	300 <i>s</i>	60 <i>s</i>
Memory Required	1.14 <i>GB</i>	1.14 <i>GB</i>	0.96 <i>GB</i>

transferred data to around 10 – 100 *KB* instead of gigabytes and enables to implement a closed loop deformable mirror control system.

After we have solved a problem with data storage we can focus on the core of every Avionics subsystem - its processor. Now we have higher but still reasonable requirements for processing power according to the computation tasks that it will be solving: 1. Centroid, delta x and delta y, slope reconstruction, and 2. Linear algebra for mirror controller. The Steepest Ascent Mission Interface Computer CS-MIC-G-EM is a good fit for such tasks because it has an FPGA to be configured for image processing and a microcontroller for general tasks such as telemetry and ADCS computations.

3.4.3 Decisions Made - VE

We have made a decision to use CS-MIC-G-EM (Figure 18) mainly because it enables on-board image processing which reduces the amount of data we send to the ground and provides with a capability to build a closed loop deformable mirror control system.



Figure 18: Mission Interface Computer CS-MIC-G-EM [15]

It is also capable of providing the following interfaces with other subsystems see Table 8.

3.4.4 Analysis - VE

The system architecture in general is shown in Figure 19. The Mission Interface Computer we have selected allows us to separate telemetry from image processing data. The first is processed on CPU while the latter is done on FPGA.

3.4.5 Summary of Outputs - ZC

The Avionics system had very few outputs to the other subsystems. It had to give values to Thermal for operational temperature range for the computer which is -25°C to 85°C . The survival temperature is unknown. It also had to give outputs to power for power consumed during the different modes, and to structures for the mass and volume. These outputs, or budgets are detailed in Table 9.

Table 8: Avionics hardware interfaces with other subsystems (*assuming update 10 times per second).

Subsystem	Component	Interface	Data rate
Payload	Detector (IDS UI-5241LE-M)	GbE	550 <i>Mbit/s</i> max
	Mirror driver (BMC Mini-Driver)	USB 2.0	480 <i>Mbit/s</i> max
	Laser (ThorLabs CPS 186)	GPIO	–
Power	EPS, PDM	12C	400 <i>Kbit/s</i> max
ADCS	5 sun sensors	analog	100 <i>bit/s</i> *
	ADIS16305 IMU/Magnetometer	SPI	160 <i>bit/s</i> *
	Torque coils	12C (via PDM)	–
Thermal	14 Temperature Sensors	analog	100 <i>bit/s</i> *
	Thermal Heater	12C (via PDM)	–
Communication	Cadet NanoSat UHF Radio	RS232	1.5 <i>Mbit/s</i>

Table 9: This is a summary of the mass totals, power needs, and thermal needs of the avionics system.

Output	Value
Power (Standby)	0.5 <i>W</i>
Power (Data Capture)	1.25 <i>W</i>
Power (Downlink/Uplink)	0.5 <i>W</i>
Power (Safe Mode)	0.5 <i>W</i>
Mass	0.062 <i>kg</i>
Volume	0.104 <i>U</i>

3.4.6 Risks - ZC

There are two risks that avionics faces currently. One risk which is a high consequence, but a very low likelihood is that the system will not be capable of processing all of the incoming data for payload. Payload is outputting a lot of data, and because the design of the code that will do the process has not yet been done, it is unclear how quickly Avionics will be able to process incoming data. The other risk that Avionics is currently faces, which is of very low likelihood, but very high consequence, is that it will not be capable of providing the required latency for Payload or for ADCS. Research needs to be conducted to determine how fast avionics can receive and issue orders to ensure that the computer is fast enough for the system. If it is not fast enough there could be major failures in the system because the

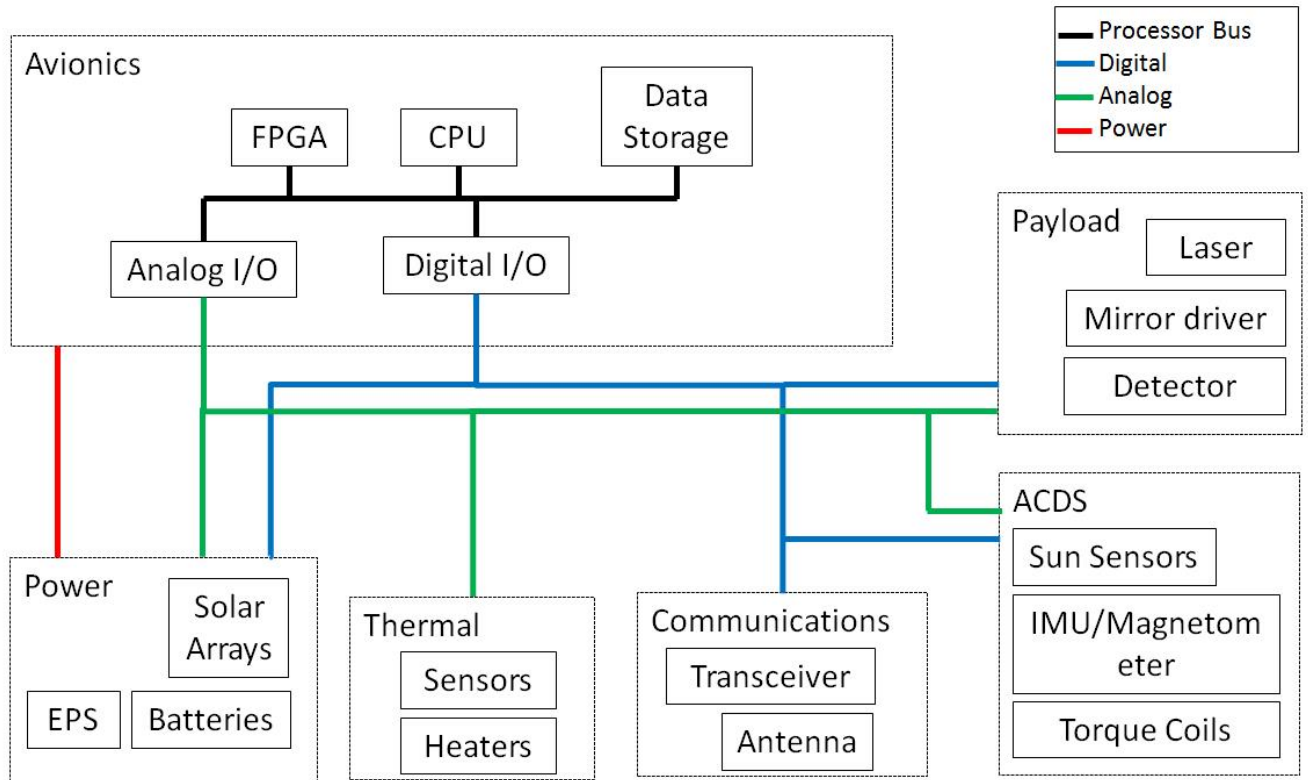


Figure 19: Caption goes here...

attitude of the craft is not correct.

3.4.7 Future Work - ZC

The future work that needs to be conducted is that there should be work done to determine a new solution to interfacing with Payload. The mirror driver interfaces with USB 2.0, however the computer is not able to interface with this. So work should be done into determining how to resolve this. One other thing that should be looked into is ensuring that the system can run all of the necessary calculations at the required speed so that all of the payload data can be processed and sent to the ground. If all of the data cant be processed, it would be difficult to complete our science goals.

3.5 Attitude Determination and Control System

3.6 Thermal - Tam? David?

3.6.1 Requirements

The requirements of the thermal subsystem were as follows:

- THM1: The thermal subsystem shall ensure that all components are kept within their survival temperature ranges for the duration of the mission.
- THM2: The thermal subsystem shall ensure that all operating components are kept within their operating temperature ranges.
- THM3: Monitor the temperatures of all key components.

3.6.2 Analysis/Results

The analysis of the thermal environment of the satellite took into consideration the radiation fluxes from the sun and earth (albedo and infrared) on all six faces of the cubeSat as shown in Figure 20. For each face, an energy balance was carried out and the average energy over all faces used to determine the average temperature of the satellite. The energy balance equations were as follows:

$$Q_{in} + Q_{internal} = Q_{out} \rightarrow [\alpha(S + S_A) + \epsilon S_{IR}]A + Q_{internal} = A_S \epsilon \sigma T^4 \quad (18)$$

Values for radiation flux over the course of an orbit were taken from the new SMAD, the main text for this course. Temperatures were calculated for two extremes, cold case, $\beta = 0$; hot case, $\beta = 45$, where β is the angle subtended by the orbit relative to the sun.

Figure 20: Thermal environment of satellite considered in analysis.

The operating and survival temperatures of other subsystems are shown in Table 10. These figures were used to determine the desired temperature range of the satellite during each mode of operation. The results of the analysis are shown in Table 11. These show that during the cold case, the satellite will experience temperatures below the operation and survival temperatures of the payload during data-capture and other modes respectively.

Table 10: Operating and survival temperatures of different subsystems and components.

Equipment	Operating Temperature (°C)	Survival Temperature (°C)
Payload	0 to 35	-10 to 70
ADCS	-20 to 40	-20 to 40
Avionics	-25 to 85	-25 to 85
Batteries (have internal heaters)	0 to 50	-10 to 50
Solar Arrays	-40 to 80	-50 to 100
Communications	-20 to 70	-40 to 80

Table 11: Results of the thermal analysis for hot and cold cases.

Mode	Data Capture	Standby	Uplink	Downlink	Safe
Operating temp. (°C)	0 to 35	-10 to 40	-10 to 40	-10 to 40	-10 to 40
Temp. Cold case (°C)	-3.68	-13.40	-13.40	5.79	-15.72
Temp. Hot case (°C)	21.99	14.72	14.72	29.31	13.02

3.6.3 Trade Studies

Based on the results of the thermal analysis, the need to augment the thermal control was evident. Amongst the myriad of possible options, the inclusion of a heater, multi-layer insulation (MLI aka thermal blanket), and surface coating stood out as more feasible for a cubeSat mission given the limited mass, volume, and power available. Since the payloads detector was the main component whose temperature needed to be kept above the average satellite temperature for most modes of operation, a decision needed to be made on whether a heater or thermal blanket would be used as the primary thermal control for the payload.

The heater being considered was a model HK5586 polyimide thermofoil heater from Minco (see Figure 21). It takes up an area of 4.50 cm x 2.54 cm, operates within -200 to 200 °C, and with an input voltage of 3.3V, would require a maximum wattage of 0.83 W.

Figure 21: Thermofoil heater and payload detector

Computing the heat exchange between the heater and the detector, we obtained values for the average power required by the heater to keep the detector above 0 C during data capture mode, and above -10C during other modes. The equation used:

$$P_{req} = \frac{\text{Energy transferred}}{\text{Time}} = \frac{m_{sat}Cp_{sat}(T_{min} - T_{sat})}{\text{Time}} \quad (19)$$

Where a maximum of ten seconds is allowed for the detector to attain desired temperatures, and T_{min} corresponds to the minimum operational and survival temperature during data capture and other modes respectively. The results are shown in Figure 22. Excepting downlink mode, the heater will require power ranging from 0.44 to 0.75W, which is a significant percentage of the average power available to the entire satellite.

Figure 22: Power usage by heater during different modes of operation.

For the thermal blanket option, we considered aluminized 25 gauge polyester with nylon scrim from Dunmore. Some of the advantages of this option are that it does not require power, and its mass requirement is significantly low.

In order to determine the amount of insulation needed, a lumped parameter model for the thermal diffusion through the thermal blanket was used. Temperature of the inner face of the MLI is given by

$$T = T_{\infty} + (T_i - T_{\infty})e^{-t/\tau}, \tau = m \times Cp \times R_{ext} \quad (20)$$

Where τ is the time constant for temperature decay, R_{ext} is the thermal resistance to external heat flux, and T_i and T_{∞} are the initial temperature of the inner face and average temperature of the satellite respectively. In order to achieve a time constant of approximately the duration of eclipse, two layers of insulation will be required. The results are shown in Figure 23.

Figure 23: Temperature decay of inner face of MLI for different modes of operation.

3.6.4 Design/Budget

Given the results of the aforementioned analysis, the thermal blanket was chosen for primary thermal control. Initially, the thermal subsystem chose dispense with idea of a payload heater, and use solely the MLI for thermal control, but after further discussion with other subsystems, it was agreed upon to still have the heater installed. The rationale behind this decision was that in the event that the average satellite temperature falls below the predicted value, the heater would be used to augment the action of the thermal blanket.

Thus, the design will include a double layer thermal blanket surrounding the payload, aluminized 25 gauge polyester with nylon scrim taking up approximately 1g and 0.8cm³ of

mass and volume respectively. In addition, the heater will be attached to the detector within the thermal blanket as shown in Figure 21.

Furthermore, in order to fully meet the third requirement of the subsystem, the temperatures of key components of other subsystems will be monitored via thermal sensors. These components are listed in Table 12 below.

Table 12: Key components and their corresponding number of thermal sensors required.

KEY COMPONENTS	Sensors needed
Sun sensors	5
Torque coils	3
ADCS interface board	1
DMS + Driver	1
Detector	1
Laser	1
Electronic Power System	1
Power Distribution Module	1
Total	14

The thermal sensors chosen are model 44004 precision thermistor elements from Omega, each of volume 0.04cm³ and mass 0.4g. Fourteen in all, they will each draw power of about 0.5 W and operate within a temperature range of -80 to 120 C. As shown in Figure 24 they consists of a bead and a tail; the bead will be attached to the surface of the component whose temperature is being measured, and the tail goes to the avionics board.

Figure 24: Precision Thermistor elements model 44004 (Omega.com).

In addition, the zenith and nadir faces will be painted with Chemglaze Z306 ($\alpha = 0.98, \epsilon = 0.89$) in order to improve their absorptivity-emissivity ratio from 0.9 to 1.1.

In summary, the mass, volume, and power budget will be as shown in Table 13

Table 13: Outputs (mass, power consumed, volume) to other subsystems.

	Mass (kg)	Power (W)	Volume (U)
Thermistors			
MLI			
Heater			
Surface coating			N/A

3.7 Structures

4 Conclusion - AW

In this paper it has been shown that a low-cost, quick-access mission can be carried out on a 3U CubeSat platform in order to demonstrate MEMS deformable mirror technology on-orbit. Continued iterations of the system design based on the current system risks and outlined in the section on future work need to be carried out in order to optimize the design.

4.1 Risk Summary - AW

Although, at this stage in the design the DeMi demonstration system closes, the mission is still confronted with a number of risks (see Figure 25). Due to the fact that there is only a 9% margin instead of an 18% margin between the power required and the power that can be supplied to the system, there is a high consequence, medium likelihood risk (PO1) that there will not be enough power to supply the system in order to carry out the mission.

There is also a risk (S1) that the center of mass of the structure could move out of range. With the current design, the center of mass is within range. However, since at this stage in the design there still exists the possibility that masses and positions of the parts may change, the center of mass could potentially move out of range. This risk is low likelihood but high consequence.

Two risks exist regarding the avionics subsystem. The first, a low likelihood, high consequence risk (AV1), is that the avionics subsystem will not be capable of processing all of the incoming data. The second (AV2), regards the avionics system not being capable of providing the required latency for the Payload and ADCS subsystems.

Additionally, there is a low consequence, low likelihood risk (AD1) that ADCS will exceed the system mass budget. Since a trade between mass and power was made in the design of the torque coils, both the mass and power budgets of the system are tight, and the system components and design still have the potential to change in this stage of the design, if the torque coil design needs to change in order to reduce the power draw of the system, the mass might increase to above the maximum set by the CubeSat regulations. However, this is a low consequence, low likelihood risk since currently the system mass is under the maximum for a 3U CubeSat with over a 30% margin.

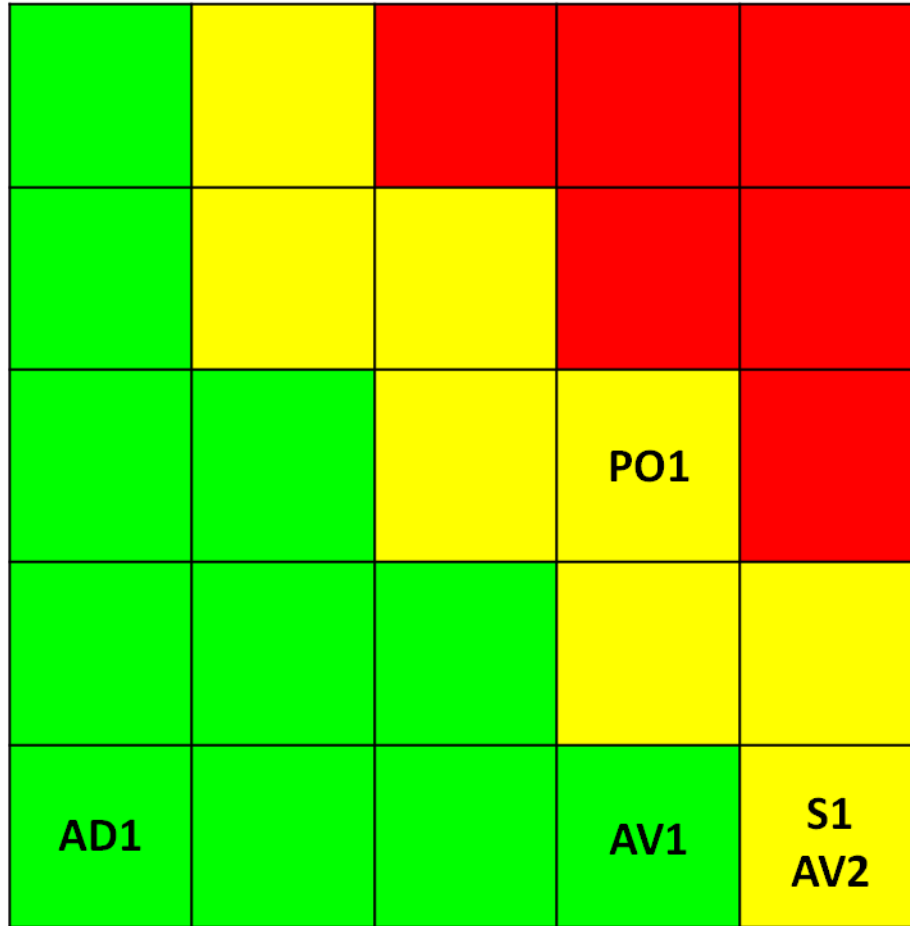


Figure 25: Systems level risk chart.

4.2 Future Work - AW

More iterations in the design process need to be carried out before the design can be completed. Future work for the DeMi demonstration includes creating more detailed models of the temperature dependence of battery and solar panel performance and the temperature gradient across the satellite in order to more accurately calculate the power that can be supplied to the system and to determine whether the proposed heating design will be effective. Additionally, as the design continues to mature, the structural model will need to continue to be updated. It also needs to be verified that the structure and components will survive the launch environment. In addition, further research needs to be conducted on the construction and use of the measuring tape antenna. More research and analysis needs to be carried out regarding the interface with payload and it must be confirmed that the avionics system can

process all information at the required speed. Finally, ADCS needs to create more accurate models of external disturbances and an attitude control loop.

4.3 Attitude Determination and Control System (ADCS) - TN

4.3.1 Requirements

The two main driving requirements for the ADCS subsystems are the pointing requirement (15°) for communication purpose and the stability requirement ($0.08^\circ/\text{s}$) for the payload operation while imaging an external source. Another requirement is the time for the satellite to detumble and establish ground station access before starting operation modes. This duration is required to be less than 30 days, creating a secondary requirement on the total detumbling time, which is dependent of the ADCS system.

4.3.2 Trade Studies

Several control methods were considered in the design process of the ADCS system: passive magnetic control, active magnetic control, and control using reaction wheels. The main trades to be considered are mass, power usage, pointing accuracy, and pointing stability capability.

In passive magnetic control, restoring torque is generated through the alignment of the satellite magnetic moment with the local geomagnetic field. The magnetic moment is created through the use of permanent magnets. Hysteresis rods are used for vibration damping. This control option requires low mass and no power. Based on past CubeSat missions, the pointing accuracy of a passive magnetic control system in the same scale as DeMi can achieve $10-20^\circ$ [SMAD, cubesat survey], sufficient for communication requirement purpose. However, there are limitations in the ability to stabilize the satellite. Passive magnetic control systems stability performance is not reliable as the hysteresis rods do not provide fast and robust vibration damping. The expected stability achieved by this method is $1^\circ/10^\circ/\text{s}$ [cubesat survey]. Since the satellite will only have access to the external sources for a short amount of time, this method is not practical for capturing light from the stars. In addition, this control method limits the possible orientation of the satellite to only the direction along the local magnetic field. In a LEO orbit of 40° inclination such as that of DeMi, the direction of the local magnetic field varies at different orbital parameters, causing difficulties in placing antenna and external source aperture so that ground station access and external source capture can be guaranteed.

Reaction wheels provide robust 3-axis stabilization control of the satellite. This control mechanism provides high accuracy (0.0001°) in pointing direction and quick response in vibration damping providing high stability ($0.05^\circ/\text{s}$). However, the necessary sensors and actuators require high mass and power usage. The main mass contribution and power draw are from the reaction wheels. In addition, magnet torquers are also needed to desaturate reaction wheels, adding more mass and power strain on the system. This option is not practical for a small satellite such as DeMi.

Active magnetic control was chosen for this mission due to the low mass and low power requirement and sufficient attitude control performance for both communication requirement and payload science operation. According to documentation on the attitude control system of the 1U CubeSat COMPASS-1 from the University of Applied Sciences, Aachen, Germany, 3 magnetic coils of magnetic moment of $0.097 \text{ A} \cdot \text{m}^2$ can achieve a pointing accuracy of 8° [reference]. The torque coils can be sized to generate enough torque for a 3U CubeSat. The details of this calculation will be presented in the decision made and analysis section. The stability of this control method is estimated to be $< 0.12^\circ/\text{s}$, according to the ION 2U CubeSat from the University of Illinois [ref.]. The implementation of the active magnetic control the ION mission only includes magnetometer as sensor with low magnetic moment in each torque coils. The performance of the active magnetic control method is expected to improve significantly with the use of more accurate sensors, such as an IMU and sun sensors, and torque coils with higher magnetic moment. More analysis and testing will be needed to determine the stability of the system.

4.3.3 Decision Made

Orientation The satellite will be in nadir pointing orientation with the nadir face being one of the two 10 cm x 10 cm faces. This orientation can be easily achieved by active magnetic control through sending control commands based on sensors readings to the active actuators. The 3U structure of the satellite provides gravity-gradient stability along the long axis in the nadir pointing configuration. By placing an antenna on the nadir face, this orientation facilitates access to the ground station. The satellite will travel with a corner-first configuration, to optimize the amount of power acquired from solar panels (see power section for more details). The orientation of the satellite is illustrated in Figure 26 below.

ADCS sensors and actuators A summary of the sensors and actuators used in the ADCS is presented in Table 14 below.

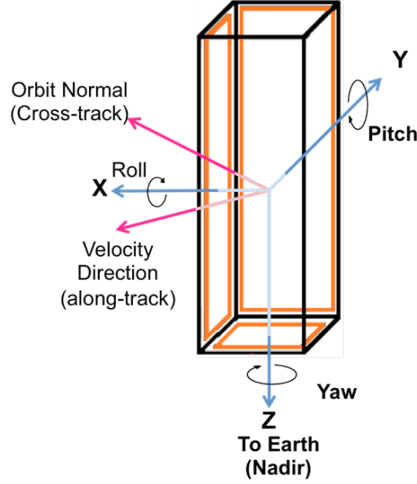


Figure 26: Satellite orientation with respect to nadir direction and velocity vector

Table 14: ADCS Sensors and Actuators

Sensors/Actuators	Quantity	Vendor	Performance
Sun sensors	5	CubeSat shop	- Field of view: 114° - Accuracy: $< 0.5^\circ$
Magnetometer	1	Analog Devices (ADIS16405)	- Dynamic range: 3.5 gauss - Initial bias: 4 mgauss
IMU	1	Analog Devices (ADIS16405)	- Dynamic range: $300^\circ/\text{s}$ - Initial bias: $3^\circ/\text{s}$ - In-run bias stability: $0.007^\circ/\text{s}$
Torque coils	3	N/A	- Max magnetic moment: 0.060, 0.063 Am^2

For attitude knowledge, a combination of sensors was chosen: sun sensors, magnetometers, and IMU. The sun sensors are low mass and low power attitude sensors that provides accurate sun angle during day time, providing the orientation of the satellite relative to an inertial frame. 5 sun sensors will be places on the faces of the satellite other than the nadir face. This sensor, from CubeSat shop provides an accuracy of $< 0.5^\circ$ and a wide field of view of 114° . The magnetometer will be used to measure the local geomagnetic field to compute the magnetic moment needed to generate needed restoring torques. In addition, the magnetometer will be used as the main attitude sensing device during eclipse periods. An IMU is used to measure the angular rate of the satellite to provide more accurate vibration knowledge to yield a robust vibration damping control loop. The IMU and magnetometer are in the same sensor unit from Analog devices. Both sensors have initial biases that can

be corrected through computation.

For actuation, 3 custom-made orthogonal torque coils will be used for 3-axis stabilization control. The coils will be sized so to meet the mass and power constraint of the satellite and to provide sufficient magnetic moment to counter environmental disturbances. More detailed calculation will be presented in the analysis section. The specifications of the torque coils are presented in Table 15 below.

Table 15: Torque coils specifications

Direction	Z	X, Y
Size	10 cm 10 cm	10 cm x 30 cm
Quantity	1	2
Turns	500	300
Current	0.12 A	0.07A
Wire Gauge	28 AWG	28 AWG
Magnetic moment	0.60 Am^2	0.63 Am^2

System Schematics and Interfaces The system schematics are shown in Figure 27. The IMU/magnetometer unit, which will be mounted on an interface board, and the sun sensors will be read out through the analog channels of the power distribution module. The module will be used as an interface to the avionics subsystem. The attitude knowledge data will be processed in the avionics subsystem. Combining with the local magnetic field, the magnetic moment vector needed for the torque coils can be computed. This information will be sent to the torque coils through the Power Distribution Module (PDM), into the torque coil driver, which consist of a current driver and an H-bridge, which controls the current in each coils and their directions.

4.3.4 Analysis

Environmental Torque Calculation The main environmental disturbances on orbit are gravity gradient, magnetic field, aerodynamics drag, and solar radiation pressure. The governing equations of these external sources are presented in details in SMAD ADCS section. Using the satellite properties, these values can be computed and presented in Table 16.

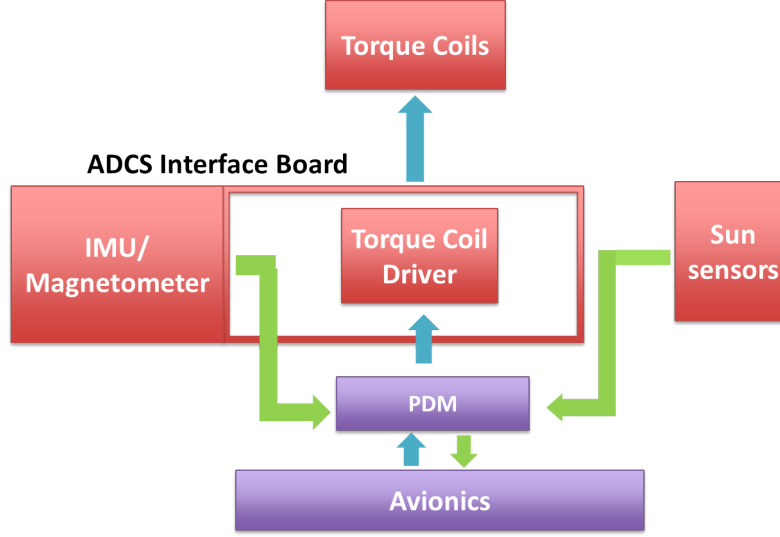


Figure 27: ADCS components interactions and Avionics interface

Table 16: Maximum Environmental Torque Estimation

Gravity Gradient	1.60E-08 Nm
Magnetic Field	1.80E-05 Nm
Atmospheric Drag	2.70E-07 Nm
Solar Pressure	5.50E-09 Nm
Total Torque	1.80E-05 Nm

Torque coil sizing calculation Magnetic control relies on the torque provided by the aligning of the satellite magnetic moment and the local magnetic field. Equation 21 shows the governing equation of magnetic control, where \vec{T} represent the generated torque vector, $\vec{\mu}$ is the satellite magnetic moment, \vec{B} is the local geomagnetic field vector.

$$\vec{T} = \vec{\mu} \times \vec{B} \quad (21)$$

Taking the torque vector to be the total environmental torque, Equation 21 above yields the required maximum magnetic moment of the coils to be $0.6Am^2$. Since the area of each coil is chosen to be the same as the size of each of the face of the satellite, the main trade of the design is the number of turns and current in each coil. This corresponds to a mass/power trade. The results of the torque coil sizing are presented above in Table 15 in Decision Made section.

Detumbling Analysis Using Princeton Satellite Systems MATLAB simulation, the momentum unloading as a response to an initial angular rate can be computed. The input parameters are the magnitude and direction of initial angular momentum, the direction of magnetic moment, and the gain of the control loop. The initial momentum was calculated by assuming an initial angular rate. The magnetic moment direction is the direction of the torque coils. The control gain is adjusted so that the maximum magnetic moments along all 3 axes are less than the maximum magnetic moments provided by the torque coils. The detumbling time can be calculated through determining the time where the momentum in all direction is less than an arbitrary low threshold.

The simulation was run with an initial angular rate of $10^\circ/\text{s}$, magnetic moment along x, y, z and a control gain of $k = 0.008$. The angular momenta and magnetic moments are presented in Figure 28.

The maximum magnetic moment needed in x, y, z are 0.6092 Am^2 , 0.6052 Am^2 , 0.0938 Am^2 , respectively, which is within the range of magnetic moment the torque coils can provide. The total detumbling time is less than 1 orbit (90 minutes).

Ground Access Duration The duration of access to ground station was computed using an STK model. The orbit was set to a LEO orbit of 500 km altitude and an inclination of 40° . The satellite configuration is set to be in nadir pointing with a possible offset of 8° . The design of the antenna is a monopole antenna of 16 cm in length. The ground station is set to NASA Wallops flight facility UHF parabolic dish of 18 m diameter. A screen shot of the STK model is presented in Figure 29.

The simulation is run over the course of a day. There are a total of 5 access opportunities of about 9 minutes each. The total ground station access time per day is about 45 minutes. The exact access duration varies with each orbit.

4.3.5 Summary of Budgets

The mass, power, and volume budgets of the ADCS system are presented in Table 17

4.3.6 Risks

The main design risk in the ADCS system is the pointing stability requirement and the mass and power budget. As previously mentioned, the stability of the satellite will need to be $\leq 0.08^\circ/\text{s}$ for payload science operation of capturing light from a star. The sensors and actuators are expected to provide this performance based on the survey of past CubeSat

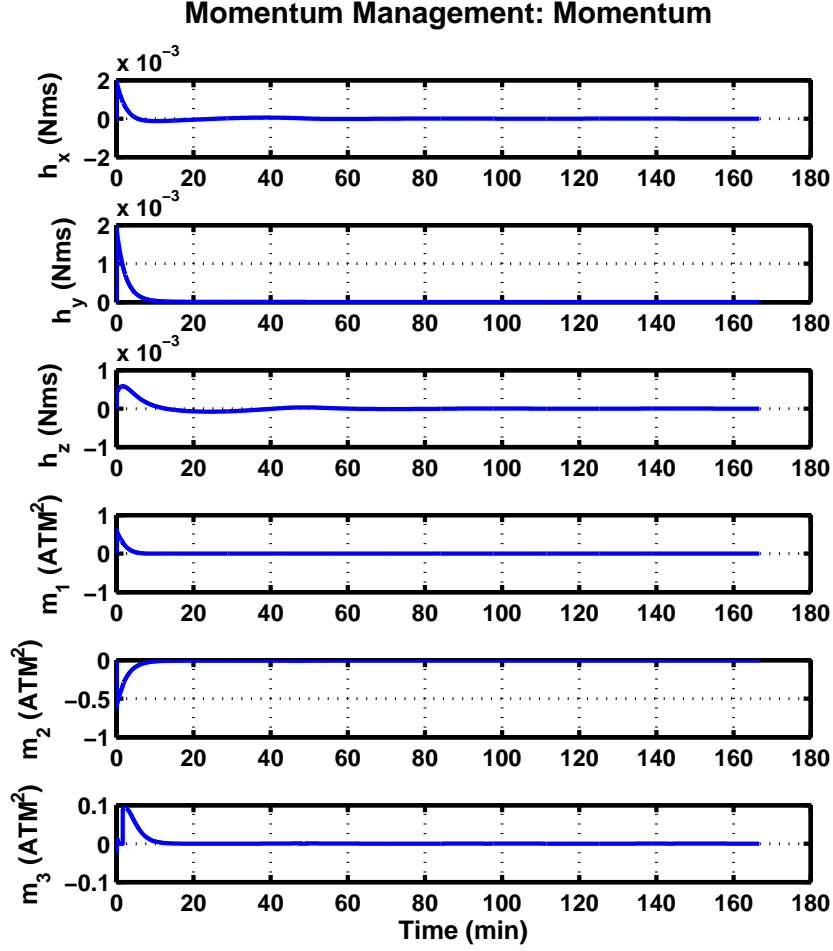


Figure 28: Momentum and magnetic moment during detumbling period

missions. However, more analysis through simulation and testing will need to be implemented to determine the exact performance of the system. The second risk is due to the narrow margin on the power budget of the whole system. To compensate for this, the mass of the torque coils is higher than previously expected. More iterations will be needed to determine the optimal power consumption and mass of the torque coils.

4.3.7 Future Work

The main future work of the ADCS system is to simulate the flight condition through with external disturbance torques at each position on orbit. The next step would be to create a control loop that takes these environmental torques as inputs to compute the needed

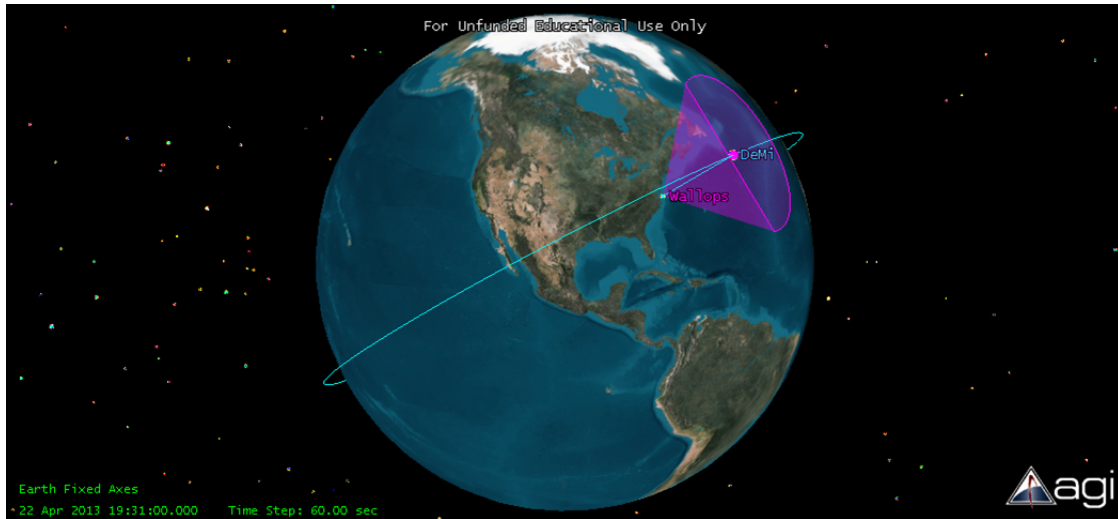


Figure 29: Ground access STK model

Table 17: ADCS budgets

Component	Volume	Mass	Power
IMU/Magnetometer	4.49 cm^3	0.016 kg	0.21 W
Sun sensors	6.530 cm^3	0.02 kg	0.25 W
Torque coils	58.32 cm^3	0.52 kg	1.35 W
Interface board	248.0 cm^3	0.17 kg	—
Total ADCS system (with margin)	318 cm^3 (0.318 U)	0.73 kg	1.81 W

magnetic moment of each of the 3 torque coils.

4.4 Thermal

4.5 Structure

5 Conclusion

5.1 Risk Analysis

5.2 Future Work

6 Acknowledgment

A

Requirements

Requirements go here.

B

Link Budgets

Figure 30: Uplink Budget

Uplink Budget					
Item	Symbol	Units	Worst Case	Best Case	Source
frequency	f	GHz	0.45	0.45	Hardware
wavelength	lambda	m	0.667	0.667	Lambda=c/f
propagation path length	r	km	2082	500	Mission/ITU-R P.676-9 eq 17, 18, 19
data rate	R	bps	19200	19200	Hardware
data rate	R	dB	42.833	42.833	
transmit antenna diameter	D_t	m	18.29	18.29	Wallops
transmit antenna beam width	theta_t	deg	2.9	2.9	Wallops
transmitter power	P	W	1	2	from DICE mission
transmitter power	P	dBW	0	3.010	
transmit antenna gain	G_t	dBi	35	35	Wallops
transmit antenna pointing offset	e_t	deg	1	0	
transmit antenna pointing loss	L_pt	dB	1.5	0	Antenna Gain Pattern
transmitter line loss	L_l	dBW	1	0.5	Line Loss for Coax Cable < http://www.arrg.us/pages/Loss-Calc.htm >
equivalent isotropic radiated power	EIRP	dBW	32.5	37.510	SMAD 16-20
receive antenna efficiency	eta		0.5	0.5	approximate efficiency
receive antenna beam width	theta_r	deg	65	65	Antenna Gain pattern
receive antenna gain	G_r	dBi	-4	3	
receive antenna pointing offset	e_r	deg	5	1	SMAD
receive antenna pointing loss	L_pr	dB	3	0	
space loss	L_s	dB	151.884	139.494	SMAD 16-22
Dry-air and water vapor loss	L_atm	dB	0.02	0.02	ITU-R P.676-9 Figure 6
total loss	L_comb	dB	157.404	140.014	
Sky Temperature	T_sky	K	60	30	
Ground Temperature	T_ground	K	290	290	
Antenna Temperature	T_antenna	K	117.5	95	Pozar Eq
Receiver Temperature	T_receiver	K	3270	3270	Hardware
System Noise Temperature	T_s	K	3387.5	3365	Pozar Eq
System Noise Temperature	T_s	dB	35.299	35.270	
receiver G/T	--	dB	-39.299	-32.270	SMAD 16-27
Boltzmann constant	k_b	dB	-228.599	-228.599	--
C/N0	--	dB	64.397	93.826	SMAD 16-30
Eb/N0	--	dB	21.563	50.993	SMAD 16-31
Bit Error Rate	BER	%	10^-5	10^-5	
Required Eb/N0	--	dB	9.5	9.5	SMAD figure 16-16
margin	--	dB	12.064	41.493	SMAD 16-33

Figure 31: Downlink Budget

Downlink Budget					
Item	Symbol	Units	Worst Case	Best Case	Source
frequency	f	GHz	0.465	0.465	Hardware
wavelength	lambda	m	0.645	0.645	Lambda=c/f
propagation path length	r	km	2082	500	Mission/ITU-R P.676-9 eq 17, 18, 19
data rate	R	bps	1500000	1500000	Hardware
data rate	R	dB	61.761	61.761	
transmit antenna length	l	m	0.164	0.164	quarter-wave monopole
transmit antenna beam width	theta_t	deg	65	65	Antenna Gain Pattern
transmitter power	P	W	1	2	from DICE mission
transmitter power	P	dBW	0	3.010	
transmit antenna gain	G_t	dBi	-4	3	
transmit antenna pointing offset	e_t	deg	5	1	SMAD
transmit antenna pointing loss	L_pt	dB	3	0	
transmitter line loss	L_l	dBW	-1	-0.8	Line Loss for Coax Cable < http://www.arrg.us/pages/Loss-Calc.htm >
equivalent isotropic radiated power	EIRP	dBW	-6	6.810	SMAD 16-20
receive antenna efficiency	eta	--	0.5	0.5	approximate efficiency
receive antenna beam width	theta_r	deg	2.9	2.9	Wallops
receive antenna gain	G_r	dBi	35	35	Wallops
receive antenna pointing offset	e_r	deg	1	0	
receive antenna pointing loss	L_pr	dB	1.5	0	Antenna Gain pattern
space loss	L_s	dB	152.169	139.778	SMAD 16-22
Dry-air and water vapor loss	L_atm	dB	0.02	0.02	ITU-R P.676-9 Figure 6
total loss	L_comb	dB	155.689	138.998	
Sky Temperature	T_sky	K	290	290	
Ground Temperature	T_ground	K	60	30	
Antenna Temperature	T_antenna	K	232.5	225	Pozar Eq
Receiver Temperature	T_receiver	K	66	66	Wallops
System Noise Temperature	T_s	K	298.5	291	Pozar Eq
System Noise Temperature	T_s	dB	24.749	24.639	
receiver G/T	--	dB	10.251	10.361	SMAD 16-27
Boltzmann constant	k_b	dB	-228.599	-228.599	
C/N0	--	dB	77.161	106.772	SMAD 16-30
Eb/N0	--	dB	15.400	45.011	SMAD 16-31
Bit Error Rate	BER	%	10^-5	10^-5	
Required Eb/N0	--	dB	9.5	9.5	SMAD figure 16-16
margin	--	dB	5.900	35.511	SMAD 16-33

References

- [1] Image from Clyde Space. URL http://www.clyde-space.com/cubesat_shop/solar_panels_-_deployable, (visited May 05, 2013).
- [2] (2012). “CubeSat Kit – In Space.” URL <http://www.cubesatkit.com/content/space.html>, (visited May 05, 2013).
- [3] Strain, A, (February 14, 2011). “User Manual: CubeSat 3U Electronic Power System.” URL <http://www.clyde-space.com/documents/2471>, (visited May 05, 2013).
- [4] Worrall, K, (March 14, 2011). “CubeSat Power Distribution Module User Manual.” URL <http://www.clyde-space.com/documents/2560>, (visited May 05, 2013).
- [5] McLaren, V, (April 28 2010). “User Manual: Standalone 30Wh Battery.” URL <http://www.clyde-space.com/documents/1902>, (visited May 05, 2013).
- [6] (March 16 2012). “CubeSat Solar Panels.” URL <http://www.clyde-space.com/documents/2625>, (visited May 05, 2013).
- [7] Cahoy, K. L., A. Marinan, B. Novak, C. Kerr, M. Webber. *Wavefront control in space with MEMS deformable mirrors*, Photonics West, MEMS Adaptive Optics VII, Vol. 8617, SPIE, Washington, D.C., 2013.
- [8] Demtroeder, W. *Laser Spectroscopy: Basic Concepts and Instrumentation*, 3rd ed. Berlin: Springer-Verlag, 2003.
- [9] DICE (Dynamic Ionosphere CubeSat Experiment), DICE-1 and DICE-2, eoPortal, <https://directory.eoportal.org/web/eoportal/satellite-missions/d/dice>, Accessed 4/2013.
- [10] Greivenkamp, John E. *Field Guide to Geometrical Optics*, Bellingham, WA: SPIE, 2004. Print.
- [11] “JPL LMRST Antenna Deployment Test”, <http://www.youtube.com/watch?v=DSvHKzM8scc>, Accessed 4/2013.
- [12] “ITU-R P.676-9”, http://www.itu.int/dms_pubrec/itu-r/rec/p/R-REC-P.676-9-201202-I!!PDF-E.pdf, Accessed 4/2013.

- [13] Nicoletta, C. A. and A. G. Eubanks. *Effect of Simulated Space Radiation On Selected Optical Materials*. Washington, D.C.: National Aeronautics and Space Administration, 1972.
- [14] Pozar, David M., *Microwave and RF Design of Wireless Systems*, Wiley, New York City, NY, 2001.
- [15] Clyde Space. CubeSat Shop. [Online]. http://www.clyde-space.com/cubesat_shop/obdh/364_mission-interface-computer-grande-em, visited May 5, 2013.
- [16] Tyson, Robert K. and Benjamin W. Frazier. *Field Guide to Adaptive Optics*. Bellingham, WA: SPIE Press, 2012. Internet resource.
- [17] Wertz, James, *Space Mission Engineering: The New SMAD*, Microcosm Press, Hawthorne, CA, 2011.